



Repositorio Institucional de la Universidad Autónoma de Madrid

<https://repositorio.uam.es>

Esta es la **versión de autor** del artículo publicado en:

This is an **author produced version** of a paper published in:

Physical Chemistry Chemical Physics 2012, 14(31): 10853-10871

DOI: <http://dx.doi.org/10.1039/C2CP40693D>

Copyright: © 2012 Royal Society of Chemistry

El acceso a la versión del editor puede requerir la suscripción del recurso

Access to the published version may require subscription

Vibrational branching ratios in the photoelectron spectra of N₂ and CO: interference and diffraction effects

Etienne Plésiat,^a Piero Decleva,^b and Fernando Martín^{*a,c}

We present a detailed account of existing theoretical methods specially designed to provide vibrationally resolved photoionization cross sections of simple molecules within the Born-Oppenheimer approximation, with emphasis on newly developed methods based on density functional theory. The performance of these methods is shown for the case of N₂ and CO photoionization. Particular attention is paid to the region of high photon energies, where the electron wavelength is comparable to the bond length and, therefore, two-center interferences and diffraction are expected to occur. As shown in a recent work [Canton *et al.*, *Proc. Natl. Acad. Sci.*, 2011, **108**, 73027306], the main experimental difficulty, which is to extract the relatively small diffraction features from the rapidly decreasing cross section, can be easily overcome by determining ratios of vibrationally resolved photoelectron spectra and existing theoretical calculations. From these ratios, one can thus get direct information about the molecular geometry. In this work, results obtained in a wide range of photon energies and for many different molecular orbitals of N₂ and CO are discussed and compared with the available experimental measurements. From this comparison, limitations and further possible improvements of the existing theoretical methods are discussed. The new results presented in the manuscript confirm that the conclusions reported in the above reference are of general validity.

1 Introduction

Photoionization of simple diatomic molecules has been extensively investigated both from the experimental and theoretical points of view. In particular, a wealth of experimental and theoretical data has been published for total cross sections corresponding to core as well as valence-shell photoionization of the prototype N₂^{1–35} and CO^{1,2,5,6,12,13,34,36–49} molecules, from the ionization threshold up to a few tens of eV above it. More recently, the advent of high-brilliance 3rd-generation synchrotron radiation sources in combination with high energy-resolution detection techniques has opened the way for the determination of vibrationally resolved photoionization spectra of these molecules, both at low and high photon energies^{30,35,38,39,50–64}. These experimental achievements have fostered the development of new theoretical methods that, in addition to accounting for electronic degrees of freedom, are also able to describe the molecule's vibrations^{13,30,35,43,50,52,54,55,58,60,61,63–71}.

It is well known that, in general, reasonable values of total cross sections can be obtained by assuming that the nuclei are fixed at their equilibrium positions (the fixed-nuclei approximation). Obviously, this assumption is no longer valid to evaluate vibrationally resolved cross sections. In this case, one

must also calculate the electronic wave functions outside the equilibrium positions, since the nuclei move in the potential created by the electrons. This makes calculations significantly more expensive, since the electronic structure must be determined for many molecular geometries, including the equilibrium one used in the fixed-nuclei approximation.

A large number of pioneering theoretical studies have been performed by Poliakoff and coworkers, and McKoy and Lucchese. Reviews covering most early work can be found in reference⁷², and in a recent paper⁷³ (see also references therein). However, most of these studies have focused on the valence low-energy region and on the effect of shape resonances in vibrational branching ratios. Only a few of these studies have been performed in the high energy region^{58,74,75}. More recent theoretical investigations have addressed the features appearing in the photoelectron spectra at high energy, mostly in core photoionization. In particular, results for N₂ and CO obtained from these methods have led to the observation of interesting interference phenomena that are often difficult to identify in total photoelectron spectra, especially at high photon energies^{4,11,61,64,69,74–78}. Two of these phenomena, which lie at the heart of quantum mechanics, have been recently observed in vibrationally resolved photoelectron spectra from valence-shell orbitals⁷⁸: (i) two-center coherent electron emission leading to Young's type double-slit interferences⁷⁹ and (ii) electron diffraction by the molecule's atomic centers. These processes are possible because, at high photon energy, the wavelength λ_e of the ejected electron is comparable to or smaller than the size of the molecule^{80,81}; consequently, ejected electrons experience the same phenomena as

^a Departamento de Química, Módulo 13, Universidad Autónoma de Madrid, 28049 Madrid, Spain

^b Dipartimento di Scienze Chimiche, Università di Trieste, 34127 Trieste, and CNR-IOM, Trieste, Italy

^c Instituto Madrileño de Estudios Avanzados en Nanociencia (IMDEA-Nanociencia), Cantoblanco, 28049 Madrid, Spain. E-mail: fernando.martin@uam.es

normal wave do. As a result, oscillations in the photoelectron spectra are expected but they are barely observed in the total photoelectron spectra due to the rapid decrease of the corresponding cross section with photon energy⁸².

Actually there is a growing interest in such interference and diffraction patterns at high electron kinetic energies, both because of fundamental understanding of the basic phenomenon, which has been hitherto barely explored due to limitations of the previous generation sources, and because of its great potential as a means of (i) reconstructing molecular geometry and (ii) following the time evolution of the electronic cloud during chemical processes. The latter aspect has become a real possibility due to the advent of ultrashort, femto and sub-femtosecond radiation pulses produced by free-electron lasers or high-harmonic generation sources^{83–85}. While weak EXAFS oscillations in absorption cross sections due to diffraction are nowadays a standard tool for local structure determination in solid state, surface science and biological studies, comparable studies in photoelectron emission in the gas phase are just in their infancy. In fact up to now only two cases have been thoroughly explored: the diatomic homonuclear case, especially N_2 ^{4,11,61,64,69,74,75,77}, after the Cohen-Fano prediction⁸², and the HOMO/HOMO-1 oscillations in C_{60} and related systems^{86–94}. It is becoming clear, however, that such interference/diffraction patterns are an ubiquitous phenomenon, although more complex in nonsymmetrical molecules and further complicated in the valence shell by mixing of different atomic orbitals (i.e. delocalized molecular orbitals), which on the other side offer an important source of information on electronic structure and chemical effects. Actually the main experimental difficulty is to extract the relatively small diffraction features from the rapidly decreasing cross section as a function of photoelectron energy. The latter difficulty can be easily overcome by taking the ratios between two related cross sections, the neatest examples being $1\sigma_g/1\sigma_u$ emission in N_2 or the HOMO/HOMO-1 in C_{60} . Alternatively, such oscillations become apparent in angular distribution parameters⁹⁵ and in non-dipolar parameters⁹⁶, as well as in the ratios of vibrationally resolved photoelectron spectra⁷⁸. It is this latter observable that we shall explore in the present paper.

It is clear from the foregoing discussion that, although the basic mechanism is clear, quantitative interpretation of the experimental results and inversion of the experimental data to reconstruct molecular parameters will require accurate computational modeling, able at the same time to deal seamlessly all the way from diatomics to large, nonsymmetrical molecules. In this respect the theoretical approach that will be described below has already proved its capabilities for non vibrationally resolved cross sections, and appears ideally suited to the present purpose.

In this paper we present a detailed description of the theoretical methods used in reference⁷⁸ and present further evidence

of interference effects in N_2 and CO vibrationally resolved photoionization cross sections. We also show that similar conclusions are obtained by using an even more sophisticated theoretical method. Since a large number of theoretical methods making use of the fixed-nuclei approximation have been used to evaluate total photoionization cross sections at lower energies, we will also discuss the performance of the new methods for total core and valence-shell photoionization cross sections of N_2 and CO at low photon energies. Thus, for completeness, we present in section 2 a brief review of the methods that have been used in the framework of the fixed-nuclei approximation. In section 3 we describe in detail the methods based on DFT, which thoroughly used in the present work. Total and vibrationally resolved photoionization cross sections are presented and discussed in sections 4 and 5. The results obtained with the methods described in section 3 are compared with the available experimental and theoretical data at low and high photon energies and for both core and valence-shell ionization. Conclusions and perspectives are given in section 6.

2 Theoretical methods within the fixed-nuclei approximation

In this section we briefly review the methods that have been successfully used to obtain total photoionization cross sections within the fixed-nuclei approximation. Due to its simplicity, a large number of methods make use of the single-channel approximation. Among them, one of the most popular ones is the Continuum Multiple Scattering Method (CMSM) which has been used in conjunction with muffin-tin (MT) effective potentials, like the $X\alpha$ local exchange-correlation potential, as in DFT (CO, N_2 ^{11,15,34,41,43,97,98}). This method was for a long time the only one capable to treat large systems with a reasonably low computational cost and is now a standard approach in core photoabsorption studies (NEXAFS). The MT approximation is appropriate for fast electrons but introduces some non-physical effects at low energies^{99,100}. Another single channel approach is the Stieltjes-Tchebycheff moment theory (STMT) (CO^{47,101}; N_2 ^{10,30,101,102}) which is able to describe shape resonances near the ionization threshold (see results below) but suffers from limited energy resolution and range. The Schwinger iterative approach that has been implemented at the frozen core (FCHF)^{32,46,48} and relaxed core (RCHF)^{14,42,103–106} levels for polyatomic molecules can instead produce accurate solutions of the molecular electronic continuum. Another method that has been shown to provide accurate results for large systems is the present multicenter B-spline static-exchange DFT method^{17,24,33,49,107}, which makes use of the Kohn-Sham density functional theory to describe the molecular ionic states and the Galerkin approach to evaluate the continuum electron wave function in the field of the

corresponding Kohn-Sham density. One can also mention the logarithmic derivative version of the Kohn variational principle Lobatto technique (LDKL)^{12,108}, which employs multi-center GTO functions and a one center Lobatto polynomials expansion, somewhat similar in spirit.

Approaches that include additional correlation and multi-channel interactions, which are particularly important near the ionization threshold, are more sparse. Most have been implemented only for diatomics or linear molecules. The multichannel Schwinger variational method (MCS) has been extended to close-coupling wavefunctions within a configuration interaction framework^{16,18,22,25,35,109} and is able to account for electronic correlations leading to sharp resonances at low photon energy as well as more complex electronic states. Another approach based on the close-coupling expansion of the wavefunction is the R-matrix method¹¹⁰. The method has been recently used to study valence-shell photoionization of N₂²⁰. Also recently a one-center expansion method has been applied within the close-coupling approach¹¹¹. Due to their high computational cost, the latter approaches have not been used beyond the fixed-nuclei approximation.

One of the most successful approaches is based on the Random Phase Approximation (RPA), which makes use of the relaxed-core Hartree Fock (RCHF) approximation (N₂^{3,4,9,60,61,63,64,70,112–114}; CO^{76,112}) in order to describe core-orbital relaxation effects that may play an important role, e.g., in K-shell photoionization. At higher energies the RCHF approximation has also been used (CO^{43,44,50,52,54,67,115–120}, N₂³). This is in contrast with the frozen core Hartree Fock (FCHF) approximation, which has widely been used in most earlier and some recent works (CO^{42,48,58,74,75,106,121}, N₂^{22,27,32,58,74,75,106}).

A very useful alternative to include multichannel couplings is provided by the multicenter B-spline time-dependent DFT method within the linear response approximation^{24,122}. This method has been shown to provide accurate results for large systems. Earlier methods that are less employed nowadays are the multichannel quantum-defect theory (MQDT) (CO⁶⁸), the many-body perturbation theory (MBPT) (N₂^{28,123}) and the linear algebraic method (LA) (N₂²⁹).

3 DFT-like methods that account for molecular vibration

Only a few methods described in the previous section have been used to study vibrationally resolved photoionization of CO^{13,43,50,52,54,55,58,65–68,78} and N₂^{13,30,35,58,60,61,63,64,69–71,78}, and almost none in the region of high photon energies⁷⁸. The reason is that one has to evaluate electronic continuum wave functions and potential energy curves in a dense grid of internuclear distances, which makes most methods prohibitively

expensive. In this context, DFT-like methods as those described in the previous section appear as a useful alternative, since they can accurately describe continuum states resulting from core and valence-shell photoionization at a relatively moderate computational cost. In their most sophisticated version, they can even include interchannel couplings and describe some autoionization processes. They have even been used to evaluate vibrationally resolved cross section in polyatomic molecules^{124,125}. In this section, we will describe the extension of these DFT-like methods to include the nuclear motion in the Born-Oppenheimer approximation.

3.1 Vibrationally resolved photoionization cross section

The vibrationally resolved photoionization cross section is evaluated to first order of perturbation theory within the Born-Oppenheimer and dipole approximations. In the length gauge, it is given by

$$\sigma_{\alpha}(v, v'_{\alpha}, \omega) = \frac{4\pi^2\omega}{3\hbar c} a_0^2 \sum_{l_{\alpha}} |T_{\alpha l_{\alpha} v v'_{\alpha}}(\epsilon_{\alpha})|^2, \quad (1)$$

where $T_{\alpha l_{\alpha} v v'_{\alpha}}$ is the transition amplitude

$$T_{\alpha l_{\alpha} v v'_{\alpha}}(\epsilon_{\alpha}) = \int \chi_v^*(R) d_{\alpha l_{\alpha}}(\epsilon_{\alpha}, R) \chi_{\alpha, v'_{\alpha}}(R) dR, \quad (2)$$

and $d_{\alpha l_{\alpha}}$ is the dipole-transition matrix element between the initial electronic state, ψ_0 , and the final electronic continuum state, $\psi_{\alpha l_{\alpha} \epsilon_{\alpha}}$, of the molecule,

$$d_{\alpha l_{\alpha}}(\epsilon_{\alpha}, R) = \int \psi_0^*(\mathbf{r}, R) \hat{\mathbf{d}}_e \psi_{\alpha l_{\alpha} \epsilon_{\alpha}}(\mathbf{r}, R) d\mathbf{r}. \quad (3)$$

In the above equations, $\hat{\mathbf{d}}_e$ is the dipole operator, α denotes the molecular orbital from which the electron is ionized leading to the molecular ion, l_{α} and ϵ_{α} are respectively the corresponding angular momentum and energy of the photoelectron, χ_v is the initial vibrational state, $\chi_{\alpha, v'_{\alpha}}$ is the final vibrational state, and ω is the photon energy, which is related to the photoelectron energy through the equation $\epsilon_{\alpha} = \hbar\omega - IE_{\alpha}$, where IE_{α} is the ionization energy required to produce a molecular cation in with a hole in the α molecular orbital. In all cases discussed below, we will consider that transitions occur from the ground vibrational state $v = 0$ and that the irradiated molecules are randomly oriented, hence summation over x , y and z components of the dipole-transition matrix element is assumed in equation (1).

3.2 Static-exchange DFT method

To evaluate the electronic continuum state $\psi_{\alpha l_{\alpha} \epsilon_{\alpha}}$, we use an extension of density functional theory, DFT, originally developed by Decleva and coworkers to treat molecular ionization

at the molecule's equilibrium position (CO:⁴⁹ ; N₂:^{17,24,33}). In this method, bound and continuum electronic states are written as Slater determinants of Kohn-Sham orbitals calculated as described below. The method has been shown to provide accurate total photoionization cross sections for simple as well as for very complex molecules within the fixed-nuclei approximation (see, e.g.,¹²²). In order to evaluate vibrationally resolved cross sections, the method has to be extended to describe the non equilibrium geometries adopted by the molecule during its vibration. For the diatomic molecules described here, we have typically considered between 40 and 90 different geometries associated with different values of the nucleus-nucleus distance.

The first step consists in performing a standard LCAO-DFT calculation (LCAO stands for linear combination of atomic orbitals) for the ground state of the molecule by using the program ADF (*Amsterdam Density Functional*). In these ADF calculations, we use a double zeta plus polarization (DZP) basis set centered on each atom and a LB94 or LDA functional to describe exchange and correlation effects. The resulting ground state density is then used to build the hamiltonian matrix in a new basis set of B-spline functions B and real spherical harmonics Y^R :

$$\xi_{\gamma lh j}^i(r_i, \theta_i, \phi_i) = \frac{1}{r} B_j(r_i) \sum_{m=-l}^l b_{\gamma lhm} Y_{lm}^R(\theta_i, \phi_i) \quad (4)$$

where γ represents a specific irreducible representation (IR), l and m correspond to the usual angular momentum quantum numbers, h counts the number of independent angular functions with a given l in the γ IR, i indicates the i th non-equivalent expansion center, j refers to the j th B-spline, r_i , θ_i and ϕ_i stand for the spherical coordinates referred to the i center, and $b_{\gamma lhm}$ are the coefficients of the symmetry adapted linear combination of real spherical harmonics.

In order to describe correctly bound and continuum states, the radial and angular parts are expanded over several appropriate centers (see Fig. 1):

- The center of the molecule (denoted by the superscript 0), which is associated with a large sphere of radius R_{max}^0 to correctly account for the long range behavior of the continuum wave functions.
- The position occupied by each nuclei (denoted by the superscript $i \neq 0$), which is associated with a small sphere of radius R_{max}^i to accurately describe the sharpness of the bound state wave functions. This radius is generally quite small ($\approx 1a.u.$) and defined to avoid significant overlap with expansions performed on neighboring centers. Also, the last B-splines of the expansion are generally removed to force the wave function to decrease smoothly.

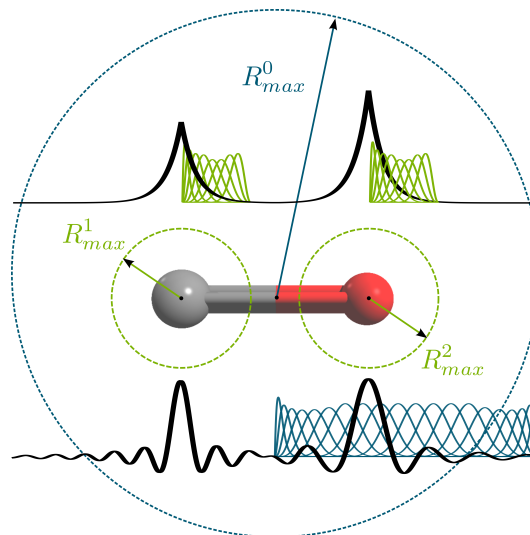


Fig. 1 Schematic illustration of the B-spline expansion used to describe bound and continuum wave functions of the CO molecule. The large (blue) and small (green) circles enclose respectively the regions where the one-center and the off-center expansions are performed. Each region has a different radius R_{max}^i . The one-center expansion is appropriate to describe the long-range oscillatory behavior of the continuum states. One of these states is represented by the thick black line in the lower part of the figure. For CO molecule, there are two non-equivalent off-centers which are located on each nucleus in order to describe the cusps of the bound states in this region. A typical bound state is represented by the thick black line in the upper part of the figure. Details of the B-spline basis set used for CO and N₂ are given in Table 1.

For a diatomic molecule, one has three centers and, consequently, the B-splines basis set is defined by the ensemble:

$$\{\xi_{\gamma}^0\} \cup \{\xi_{\gamma}^1\} \cup \{\xi_{\gamma}^2\}. \quad (5)$$

B-splines of order k are built over two different radial intervals: $[0, R_{max}^0]$ for the set $\{\xi_{\gamma}^0\}$ and $[0, R_{max}^i]$ for the sets $\{\xi_{\gamma}^i\}$ with $i \neq 0$. As mentioned above, $R_{max}^0 \gg R_{max}^i$ (see Figure 1). The Kohn-Sham orbitals are expanded on this basis set and over each center:

$$\varphi_{n\gamma} = \sum_{j=1}^{N_b} \sum_{lh} c_{n\gamma lh j}^0 \xi_{\gamma lh j}^0 + \sum_{i=1}^{\kappa} \sum_{j=1}^{N_b} \sum_{lh} c_{n\gamma lh j}^i \xi_{\gamma lh j}^i \quad (6)$$

where κ is the number of atomic centers and N_b is the total number of B-spline functions.

The LCAO basis set and consequently the cost/accuracy of the calculation is completely determined by:

- The point group symmetry of the molecule (in homonuclear diatomic molecules, the two atomic centers are identical and the explicit use of symmetry leads to a significant reduction of the computational effort).

- The B-spline parameters k , R_{max}^0 , R_{max}^i and N_b .
- The maximum value of the angular momentum l_{max}^i used in the expansion over each center i .

Actually, because of the large size of the one-center expansion with respect to the multicenter part, it is the size of the former which dominates the computational cost. For the two molecules described in this work, the details of the basis sets are given in Table 1.

The Kohn-Sham orbitals are obtained by solving the well-known equations:

$$\hat{H}_{KS}\varphi_i = \varepsilon_i\varphi_i \quad i = 1, \dots, N \quad (7)$$

where:

$$\hat{H}_{KS} = -\frac{1}{2}\nabla^2 + V_{eff}(\mathbf{r}) \quad (8)$$

and:

$$V_{eff}(\mathbf{r}) = -\sum_{i=1}^N \frac{Z_i}{|\mathbf{r} - \mathbf{R}_i|} + V_H(\mathbf{r}) + V_{XC}(\mathbf{r}) \quad (9)$$

where $V_H(\mathbf{r})$ is the electrostatic Hartree potential and $V_{XC}(\mathbf{r})$ the exchange-correlation potential. Depending on the molecular system and the properties to study, there are different choices for the potential. But it has been observed that for few-electron molecules, the LB94 and LDA functionals reproduce quite well the photoelectron spectra. In some cases, LB94 is better because it is generally more appropriate to describe the asymptotic behavior of the potential at large distances (the Coulomb tail).

Since the off-center spheres do not intersect each other, the resulting hamiltonian matrix \mathbf{H} can be partitioned into different blocks. There are diagonal blocks \mathbf{H}_{ii} connecting basis functions from the same set $\{\xi_\gamma^i\}$ and off-diagonal blocks \mathbf{H}_{i0} and \mathbf{H}_{0i} connecting basis functions from two different sets $\{\xi_\gamma^0\}$ and $\{\xi_\gamma^i\}$. The largest computational effort corresponds to calculation of the non-diagonal block elements because it is not possible to carry out integrations analytically. To evaluate the latter integrals, a numerical three-dimensional Gauss-Legendre scheme is employed.

Kohn-Sham orbitals associated with bound states are obtained by a generalized diagonalization of \hat{H}_{KS} and those associated with continuum states by block inverse iteration of \hat{H}_{KS} on a previously defined energy grid $\{E_k\}$ containing N_{E_k} points¹²². Dipole matrix elements are calculated for each partial wave, as a function of photoelectron energy and internuclear distance.

It is worth stressing here that, in contrast with standard DFT approaches in which the ground electronic density is built from the lowest KS orbitals, the present N -electron KS wave function is built from $N - 1$ KS orbitals associated with the ground electronic density and a KS orbital that lies in the electronic continuum. So, in this respect, the present

method does not have the formal mathematical support of standard DFT. In fact, it rather resembles the so-called “static-exchange” approximation, in which the close-coupling expansion of the continuum wave function containing infinite terms is truncated to a single term that is described as the anti-symmetrized product of a bound $(N - 1)$ -electron wave function and a continuum one-electron wave function. Hence the name “static-exchange-DFT”. Nevertheless, to keep the notation short throughout the manuscript, we will simply refer to it as DFT.

Table 1 B-spline basis set parameters used in the calculations reported in this work. The radii are given in a.u..

	Sym.	R_{max}^0	R_{max}^i	N_b	k	l_{max}^0	$l_{max}^{i \neq 0}$	N_{E_k}
N ₂	D _{∞h}	25.0	1.0	200	10	10	1	200
CO	C _{∞v}	25.0	1.0	200	10	10	1	200

3.3 Inclusion of the nuclear motion

The vibrational wave functions are the solutions of the Schrödinger equation

$$\left[-\frac{1}{2\mu}\nabla_R^2 + E_\alpha(R) - W_{v_\alpha} \right] \chi_{\alpha,v_\alpha}(R) = 0, \quad (10)$$

where μ is the reduced mass of the molecule, $E_\alpha(R)$ the potential energy curve associated to the α electronic state of the neutral molecule or the cation, and W_{v_α} the total energy. In this equation, molecular rotation has been ignored because energy resolution in standard photoelectron spectroscopy measurements does not allow one to resolve the rotational structure.

Equation (10) has been solved in a basis of 1000 B-splines within a box of 10 a.u.. The potential energy curves used in these calculations are obtained from different methods. The ground state of the neutral molecule and the ground and excited states of the molecular cation have been evaluated by using a multi-reference configuration interaction (MRCI) method within the complete active space self-consistent field (CASSCF) approximation. For electronic states of the cation containing a hole in the core, we have used Morse potentials using accurate spectroscopic data taken from the literature. Figures 2 and 3 show the potential energy curves used in equation (10) for the N₂ and CO molecules. In the case of the ground state of the neutral molecule, the figure illustrates a comparison between the Morse potential and calculated ab initio potential energy curve. As can be seen, both potentials are nearly identical in the vicinity of the energy minimum, thus suggesting that a Morse description of core-hole states

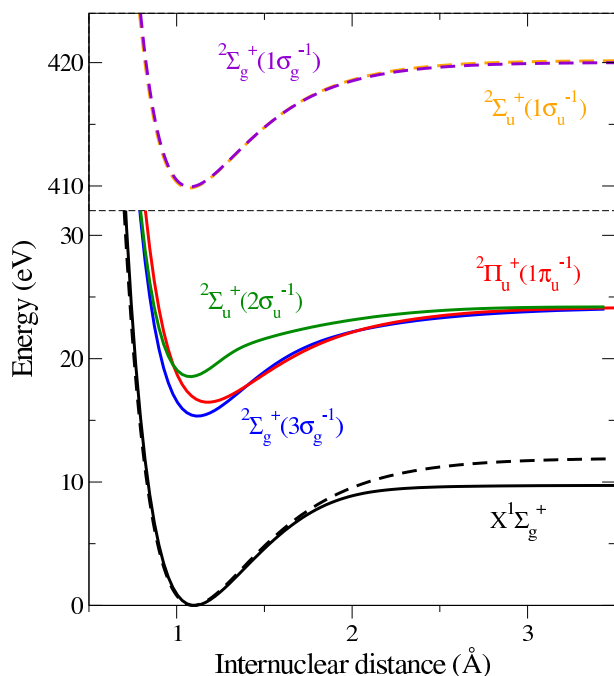


Fig. 2 Potential energy curves for the ground state of N_2 , the three first valence electronic states and the K-shell of N_2^+ . Valence electronic states (solid lines) were obtained using CASSCF-MRCI *ab initio* method and core ionized electronic states (dashed lines) are Morse potentials based on a CCSD(T) calculation from¹⁴¹.

for which standard CASSCF-MRCI calculations are not so easy to perform is accurate enough. For the ground state of the neutral and the cation, as well as for the lowest excited (valence) states of the cation, our calculated potential energy curves are in very good agreement with the ones previously reported in the literature^{7,60,65,114,120,126–140}.

3.4 Time-dependent DFT

The DFT method described in the previous paragraphs may be inappropriate when the coupling between different ionization channels is important and/or when singly- or doubly-excited Feshbach resonances, in which electron correlation plays a major role, have an important contribution. An alternative and, very often, more accurate procedure is to use time-dependent DFT (TD-DFT) at the first order of perturbation theory (i.e., as a linear response). The time-dependent DFT approach makes use of many ingredients from the time-independent DFT method. For this reason, we will only explain the concepts that are exclusive of the time-dependent approach. For a more complete theoretical overview, see for example¹⁴³.

Following the description of Zangwill et Soven in¹⁴⁴, the response potential due to a first order change in the electron

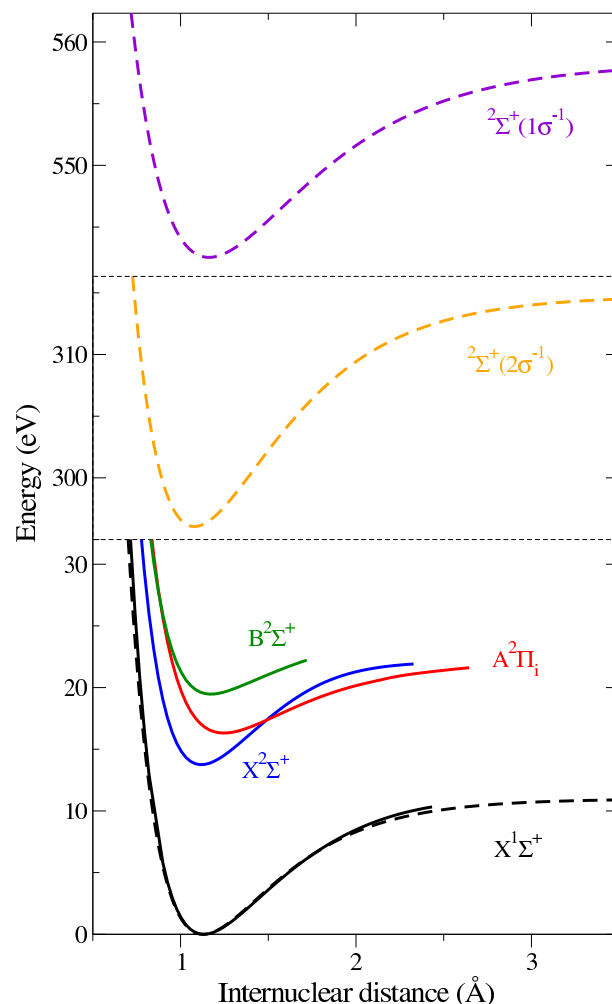


Fig. 3 Same as Figure 2 but for CO. Morse parameters were derived from experiments by Herzberg et al. reported in⁵⁶ for the ground state and by Kugeler et al. in¹⁴² for the core ionized states.

density induced by the external field is taken into account self-consistently, giving rise to a total perturbing potential V_{SCF} that is the sum of the external field potential and the induced one:

$$V_{SCF}(\mathbf{r}, \omega) = V_{EXT}(\mathbf{r}, \omega) + \delta V(\mathbf{r}, \omega) \quad (11)$$

where δV is given by:

$$\delta V(\mathbf{r}, \omega) = \int \frac{\delta n(\mathbf{r}', \omega) \mathbf{dr}'}{|\mathbf{r} - \mathbf{r}'|} + \left. \frac{\partial V_{XC}}{\partial n} \right|_{n(\mathbf{r})} \delta n(\mathbf{r}, \omega) \quad (12)$$

which includes the induced Coulomb and exchange-correlation potentials in the adiabatic local density approximation (ALDA). In the latter equation, $\delta n(\mathbf{r}, \omega)$ indicates deviations from the unperturbed density distribution induced by the applied external field. For practical purposes, equation (12)

can also be written (in an obvious notation) in terms of a kernel K acting on the induced density

$$\delta V(\mathbf{r}, \omega) = \int K(\mathbf{r}, \mathbf{r}') \delta n(\mathbf{r}', \omega) d\mathbf{r}' \quad (13)$$

The use of a LCAO basis set expansion makes the Modified Sternheimer Approach (MSA)¹⁴⁵ more suitable for the resolution of the linear response equations. In the MSA formalism, the KS eigenfunctions at the first order of perturbation $\varphi_i^{(1,\pm)}$ are calculated via the inhomogeneous equation:

$$[H_{KS} - \varepsilon_i \pm \omega] \varphi_i^{(1,\pm)} = \hat{P} V_{SCF} \varphi_i \quad (14)$$

where \hat{P} is a projector that orthogonalizes with respect to the occupied states. The induced density is then obtained as

$$\delta n(\mathbf{r}, \omega) = \sum_i n_i \left(\varphi_i^* \varphi_i^{(1,\pm)} + \varphi_i \varphi_i^{(1,\mp)*} \right) \quad (15)$$

The most efficient algorithm employs V_{SCF} as the basic dynamical variable, thus avoiding the need of SCF iterations, which are generally unstable in complex molecules¹⁴³. Defining the linear susceptibility χ as

$$\delta n(\mathbf{r}, \omega) = \int \chi(\mathbf{r}, \mathbf{r}', \omega) V_{SCF}(\mathbf{r}', \omega) d\mathbf{r}' \quad (16)$$

and projecting V_{SCF} , δn , χ , and K into the basis $\{\xi_\gamma^i\}$ transforms equation (11) into a system of linear algebraic equations in V_{SCF} , which in matrix form reads

$$[\mathbf{1} - \mathbf{K} \cdot \chi(\omega)] \mathbf{V}_{SCF}(\omega) = \mathbf{V}_{EXT}(\omega) \quad (17)$$

Notice that, since the kernel K is energy independent, the corresponding matrix elements must be computed only once. The χ matrix elements are energy dependent and must thus be computed at each photon energy by solving the inhomogeneous equation (14). In the solution of (14) for $\varphi_i^{(1,-)}$ lying in the continuum, correct boundary conditions must be enforced. Finally, once V_{SCF} is obtained, the cross section is calculated via transition moments that make use of V_{SCF} instead of the dipole operator.

A comparison of the relevant equations shows that RPA is formally equivalent to linear TD-DFT, from which it can be obtained by replacing V_{XC} matrix elements by the exchange integrals used in RPA. In general, the V_{XC} potential provides a better description of electron correlation and, for this reason, TDDFT is sometimes a bit more accurate than RPA at a substantially lower computational cost, and is often comparable to more sophisticated approaches. It must be stressed however that, although interchannel coupling and singly excited autoionizations are included, double or higher electron excitations are presently outside the scope of the approach. In many cases, the local density approximation is appropriate to treat

photoabsorption processes in “small” systems (in atoms¹⁴⁴ as well as in molecules^{78,107,124,125,143,146–148}).

In spite of this, there is an important warning to make when slow-decaying Feshbach resonances come into play. In many cases, the autoionization lifetimes of these resonances are comparable or even larger than the time employed by the nuclei to move significantly. Under these circumstances, the use of the Born-Oppenheimer approximation is not justified and may lead to wrong results. This has been clearly shown in the case of the autoionization decay of H_2 ¹⁴⁹, for which an accurate description of the experimental findings in the region of the autoionizing doubly-excited states requires going beyond the Born-Oppenheimer approximation. Therefore, although the TD-DFT approach will always do a better job than the DFT one in describing correlations due to the coupling between different open ionization channels, it is not guaranteed that it will do so when slow decaying Feshbach resonances are involved.

4 Total photoionization cross sections

In this section we will present non vibrationally resolved photoionization cross sections for photon energies going from the ionization threshold up to several hundreds eV above it. These cross sections have been obtained by summing over all the vibrationally resolved cross sections. In all transformations from photoelectron energies to photon energies and vice versa, we have used the values of the adiabatic ionization potentials given in Table 2.

Table 2 Adiabatic ionization potentials of N_2 and CO .

Photoionization		IP
N_2	$1\sigma_g^{-1}$	409.94 eV ¹⁵⁰
	$1\sigma_u^{-1}$	(g/u splitting: 101 meV ¹⁴¹)
	$2\sigma_u^{-1}$	18.558 eV
	$1\pi_u^{-1}$	16.490 eV
	$3\sigma_g^{-1}$	15.347 eV
CO	$1\sigma^{-1}$	542.54 eV ¹⁵¹
	$2\sigma^{-1}$	296.07 eV ¹⁵²
	$4\sigma^{-1}$	19.483 eV
	$1\pi^{-1}$	16.326 eV
	$5\sigma^{-1}$	13.768 eV

4.1 Valence-shell photoionization

Figs. 4 and 5 show the photoionization cross sections of N_2 and CO that correspond to electron removal from the highest-occupied molecular orbital (HOMO), the HOMO-1 and the HOMO-2 orbitals of both molecules. The photon energy range

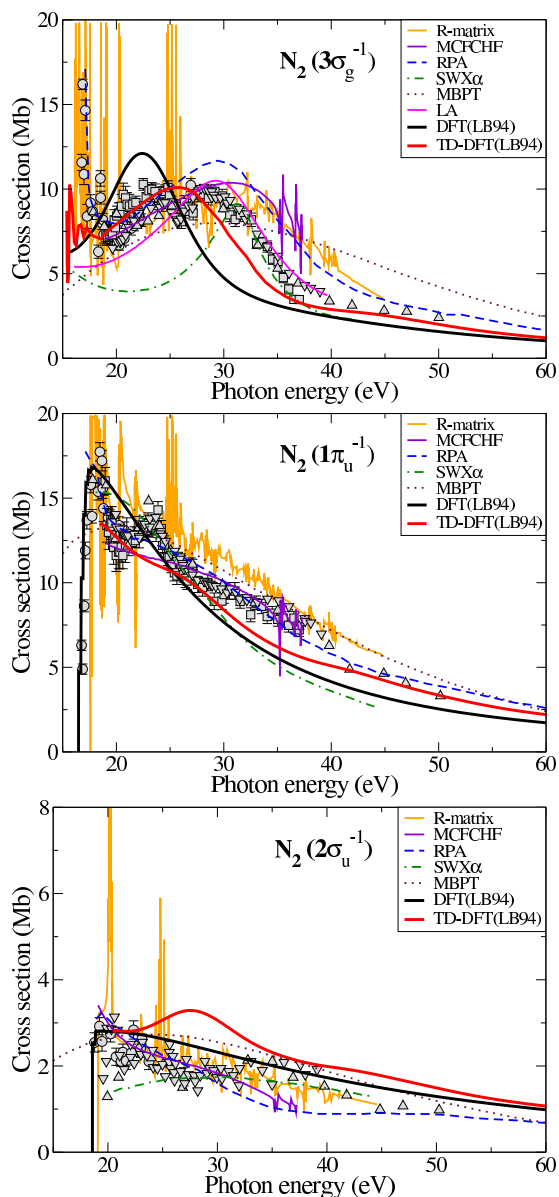


Fig. 4 Total cross section for the $3\sigma_g^{-1}$, $1\pi_u^{-1}$ and $2\sigma_u^{-1}$ photoionization of N_2 as a function of the photon energy. Symbols correspond to experiments - Circle:⁸, Square:⁷, Triangle-up:⁶, Triangle-down:⁵; Lines correspond to theory - Orange solid: R-matrix CASSCF²⁰, Violet solid: multichannel frozen-core Hartree-Fock (MCFCHF) four-channel length gauge²², Blue dashed: random phase approximation (RPA)²⁷, Green dashed-dotted: scattered-wave (SW) $X\alpha$ method³⁴, Maroon pointed: many-body perturbation theory (MBPT)²⁸, Magenta solid: Linear algebraic method (LA)²⁹, Black thick solid: multicenter B-splines time-independent DFT (DFT) method using a LB94 functional (this work), Red thick solid: multicenter B-splines time-dependent DFT (TDDFT) method using a LB94 functional (this work).

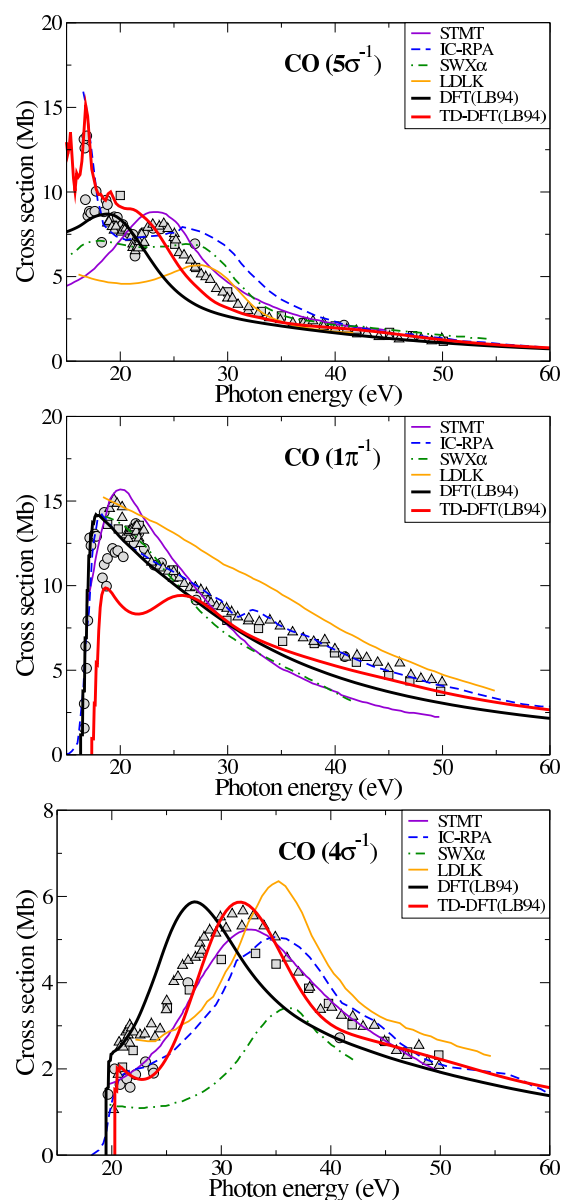


Fig. 5 Total cross section for the $5\sigma_g^{-1}$, $1\pi^{-1}$ and $4\sigma^{-1}$ photoionization of CO as a function of the photon energy. Dots correspond to experiments - Circle:⁴⁰, Square:⁶, Triangle-up:⁵; Lines correspond to theory - Violet solid: Stieltjes-Tchebycheff moment theory (STMT)⁴⁷, Blue dashed: IC random phase approximation (RPA) in the mixed gauge⁴⁹, Green dashed-dotted: scattered-wave (SW) $X\alpha$ method³⁴, Orange solid: logarithmic derivative version of the Kohn variational principle Lobatto technique (LDKL)¹⁰⁸, Black thick solid: multicenter B-splines time-independent DFT (DFT) method using a LB94 functional (this work), Red thick solid: multicenter B-splines time-dependent DFT (TDDFT) method using a LB94 functional (this work).

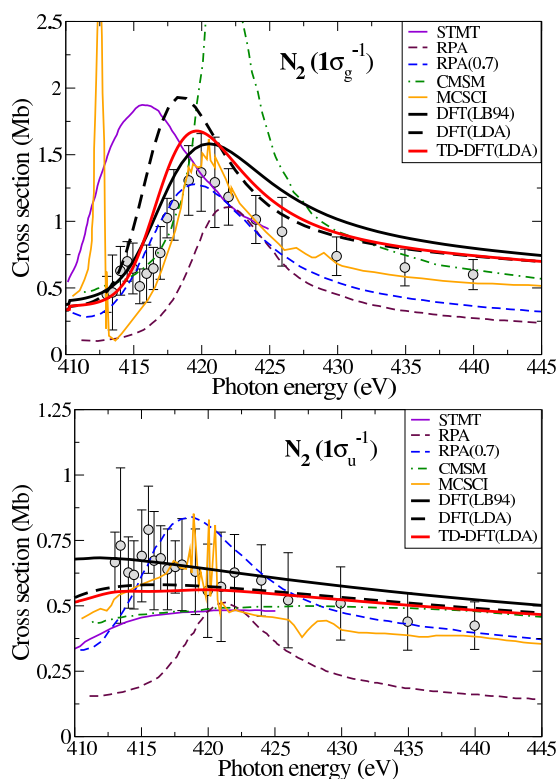


Fig. 6 Total cross section for the $1\sigma_g^{-1}$ and $1\sigma_u^{-1}$ photoionization of N_2 as a function of the photon energy. Dots correspond to experiments - Circle:⁶³; Lines correspond to theory - Violet solid: Stieltjes-Tchebycheff moment theory (STMT)¹⁰, Maroon dashed: random phase approximation (RPA)³, Blue dashed: RPA with the fractional charge basis set RCHF(0.7)⁶³, Green dashed-dotted: continuum multiple scattering method (CMSM)¹⁵, Orange solid: multichannel Schwinger configuration interaction (MCSCI) ten-channel¹⁸, Black thick solid: DFT method using a LB94 functional (this work), Black dashed thick: DFT method using a LDA functional (this work), Red thick solid: TDDFT method using a LDA functional (this work).

goes from the ionization threshold up to 60 eV. The available experimental data are compared with theoretical results previously published in the literature and with those obtained by using the DFT and TDDFT methods described in the previous section. As can be seen, results from the TDDFT method are slightly in better agreement with experiment than those from the DFT method. This is not surprising because, electrons ejected in this range of photon energies are slow and, therefore, electron correlation is expected to play a significant role. This is especially important in the vicinity of shape and Feshbach resonances, which lead to the peaks observed just above the ionization threshold. Previous theoretical methods also lead to reasonable results, although they were obtained in the fixed nuclei approximation and, in some cases, they do not

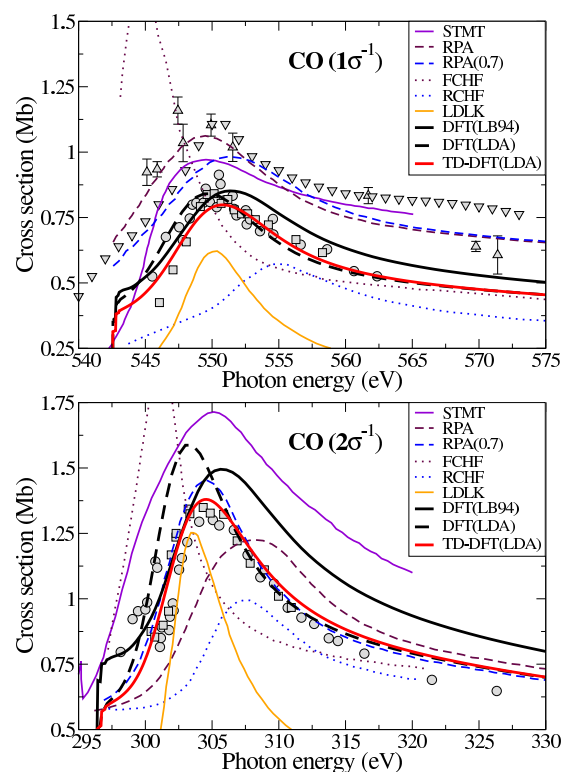


Fig. 7 Total cross section for the $1\sigma^{-1}$ and $2\sigma^{-1}$ photoionization of CO as a function of the photon energy. Dots correspond to experiments - Circle:¹⁴², Square:⁵⁵, Triangle-up:³⁶, Triangle-down:¹⁵³; Lines correspond to theory - Violet solid: Stieltjes-Tchebycheff moment theory (STMT)⁴⁷, Maroon dashed: random phase approximation (RPA)⁴⁴, Blue dashed: RPA with the fractional charge basis set RCHF(0.7)⁴⁴, Maroon points: frozen-core Hartree-Fock (FCHF) in the length gauge⁴², Blue points: relaxed core Hartree-Fock (RCHF) in the length gauge⁴², Orange solid: logarithmic derivative version of the Kohn variational principle Lobatto technique (LDKL)¹², Black thick solid: DFT method using a LB94 functional (this work), Black dashed thick: DFT method using a LDA functional (this work), Red thick solid: TDDFT method using a LDA functional (this work). (Experimental data¹⁴² and⁵⁵ were renormalized to our theoretical ones).

predict any structure near the ionization threshold. RPA results are very close to our TDDFT results and to experiment, and they also predict the existence of resonance near threshold, but one should notice that some of these RPA results were obtained by using effective charges chosen to minimize the differences with the experimental results. The many structures observed in the R-matrix results for N_2 are likely due to the presence of pseudo-resonances that are the consequence of using the fixed-nuclei approximation. These resonances are completely washed out by inclusion of the nuclear motion.

The magnitude and overall shape of the cross sections is very similar for N_2 and CO. However, resonance structures

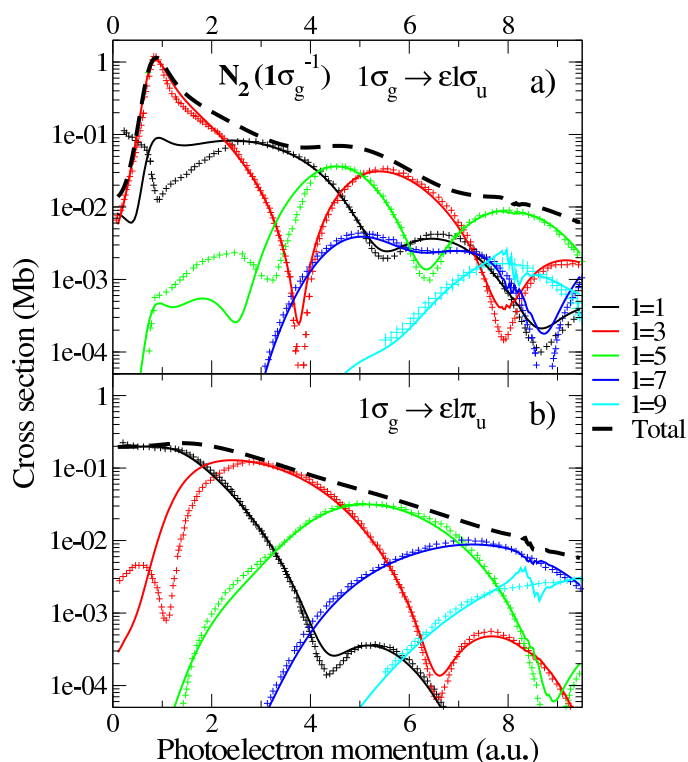


Fig. 8 Contribution of the five first partial waves to the total cross section of the $1\sigma_g \rightarrow \varepsilon l\sigma_u$ (a) and $1\sigma_g \rightarrow \varepsilon l\pi_u$ (b) transitions of N_2 as a function of the photoelectron momentum. Crosses: RPA (at $k \leq 3 a.u.$) and RCHF (at $k > 3 a.u.$) from⁶¹. Solid lines: DFT method using a LB94 functional (this work).

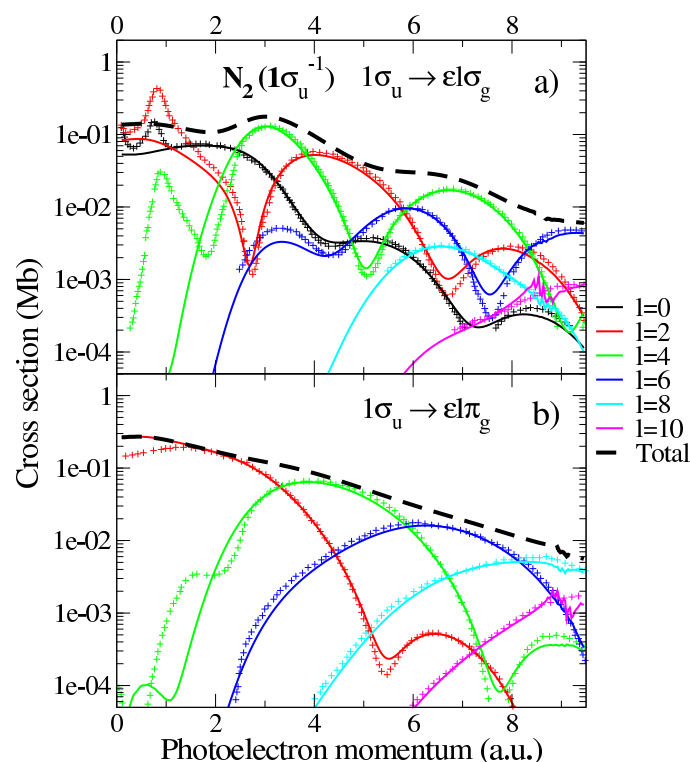


Fig. 9 Contribution of the six first partial waves to the total cross section of the $1\sigma_u \rightarrow \varepsilon l\sigma_g$ (a) and $1\sigma_u \rightarrow \varepsilon l\pi_g$ (b) transitions of N_2 as a function of the photoelectron momentum. Crosses: RPA (at $k \leq 3 a.u.$) and RCHF (at $k > 3 a.u.$) from⁶⁴. Solid lines: DFT method using a LB94 functional (this work).

near the ionization threshold are different. For instance, while experiments exhibit a pronounced peak at around 23 eV in $N_2(1\pi_u^{-1})$ photoionization, such peak is barely visible in $CO(1\pi^{-1})$ photoionization. Interestingly, the present TDDFT results predict the existence of a peak in both cases (although less pronounced than that observed in $N_2(1\pi_u^{-1})$). Also, $N_2(2\sigma_u^{-1})$ and $CO(4\sigma^{-1})$ photoionization cross sections are significantly different near threshold. While experiments for the former predict the existence of a small maximum at around 35 eV, for the latter they predict a pronounced maximum at around 32 eV. The latter maximum is very well reproduced by most existing theories, but the former is only reproduced by the present TDDFT results although 5 eV lower in energy.

4.2 Core photoionization

Figs. 6 and 7 show photoionization cross sections of N_2 and CO from the K-shell orbitals for photon energies up to ~ 35 eV above the ionization threshold. For N_2 , the K-shell is formed by the $1\sigma_g$ and $1\sigma_u$ molecular orbitals, which are separated

by only 101 meV (see Table 2) and have a strongly delocalized character. For CO , this shell consists of the 1σ and 2σ orbitals, which are separated by almost 250 eV and are almost identical to the $1s$ orbitals of O and C , respectively. As for valence-shell photoionization, the best overall agreement with the existing experimental data corresponds to the TDDFT and fitted-RPA results. All cross sections exhibit a pronounced maximum in the interval lying between 5 and 10 eV above the ionization threshold. This is due to a wide shape resonance. However, no other resonance structures are apparent in this low energy region, which is the consequence of the K-shell orbitals lying far away from the rest of the molecular orbitals, i.e., of the weak coupling with other ionization channels. The peaks resulting from the multichannel Schwinger configuration interaction (MCSCI) calculations are probably associated to pseudo-resonances that result from the use of the fixed nuclei approximation.

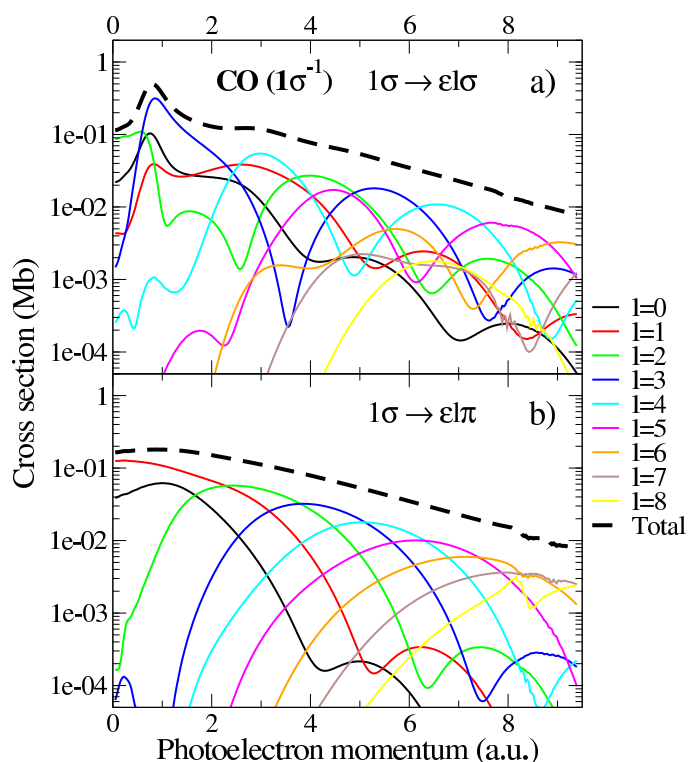


Fig. 10 Contribution of the nine first partial waves to the total cross section of the $1\sigma \rightarrow \varepsilon l\sigma$ (a) and $1\sigma \rightarrow \varepsilon l\pi$ (b) transitions of CO as a function of the photoelectron momentum. Solid lines: DFT method using a LB94 functional (this work).

4.3 Core photoionization at high photon energies

Very recently, there has been an increasing interest in evaluating photoionization cross sections at high photon energies. Figures 8 and 9 show our results for $N_2(1\sigma_g^{-1})$ and $N_2(1\sigma_u^{-1})$ photoionization and figures 10 and 11 for $CO(1\sigma^{-1})$ and $CO(2\sigma^{-1})$ photoionization. Contribution from the different partial waves is also shown. Partial waves are associated with the different angular terms in the symmetry-adapted real-spherical-harmonics expansion that describes the photoelectron wave function (see section 3.2). For example, in N_2 , a p-wave represents a continuum electron wave function with outgoing $l = 1$ character. The total cross section is just the sum over all partial waves. In general, only the few first partial waves contribute significantly to the cross section. In the present calculations, we achieve convergence by including partial waves up to $l = 9$.

In the N_2 figures, we compare our results obtained by using the DFT method (including the nuclear motion) with recent theoretical calculations reported by Semenov et al.^{61,64} in the fixed nuclei approximation. The authors employed RPA within the relaxed-core Hartree Fock (RCHF) approximation

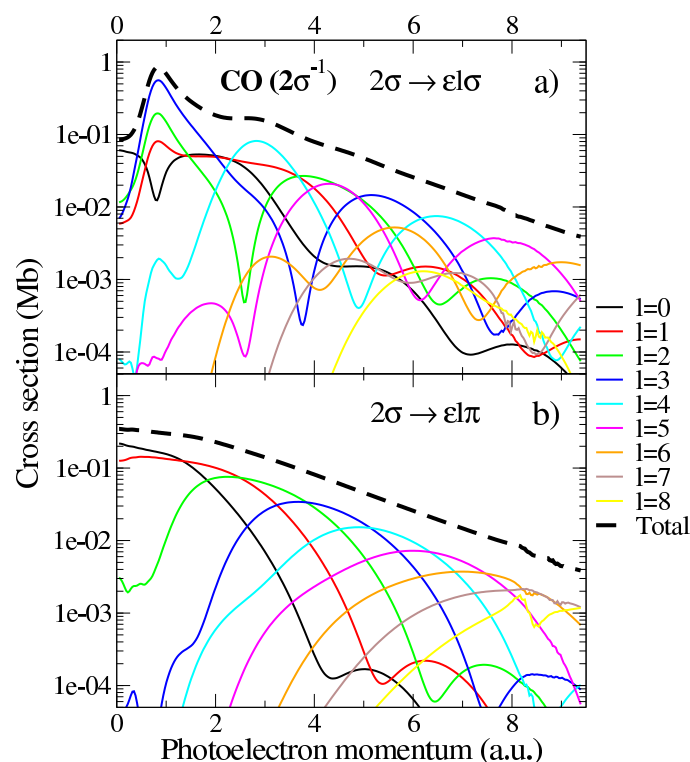


Fig. 11 Same as Fig. 10 for the $2\sigma \rightarrow \varepsilon l\sigma$ (a) and $2\sigma \rightarrow \varepsilon l\pi$ (b) transitions of CO.

at low photon energy in order to describe the strong electronic correlation in this region. RCHF is used for higher energies (> 3 a.u.). Since the authors claim that the standard RCHF method generally overestimates the influence of the relaxation effects for K-shells and give rise to a shift of the cross section toward higher energies, they make use of an adjustable parameter, the fractional charge z_e , which corresponds to some intermediate value of the charge of the hole state⁶¹. The value $z_e = 0.7$ has been empirically chosen to give the best agreement with the experimental data. For all partial waves, there is a reasonable agreement between the present DFT and the previous RPA/RCHF results, in particular at high photoelectron energies where DFT is more appropriate. Nevertheless, the RPA/RCHF methods lead somehow to sharper minima, which is the consequence of not including the nuclear motion in their calculations. A similar effect has been reported in H_2 photoionization^{80,154,155}.

The present DFT method succeeds in describing the so-called *shape resonance* for the $1\sigma_g \rightarrow \varepsilon\sigma_u$ transition at around $k_e \leq 1$ a.u. Some disagreement between RPA and DFT methods can be seen for $k_e \leq 3$ a.u. (the RPA region): for $l = 1$ (Figure 8a), $l = 3$ (Figure 8b), $l = 0, 2, 4$ (Figure 9a) and $l = 2, 4$ (Figure 9b). The difference comes from the fact that in RPA there is a significant interchannel coupling close to threshold,

as can be clearly seen in the peak appearing in the $1\sigma_u^{-1}$ cross section. Evidence of this coupling has been claimed³, but it is not apparent even in the TDDFT cross section, which formally includes this coupling, and produces an equally good agreement with the experimental data¹⁷.

The origin of the minima in the partial wave contributions can be explained in terms of electron confinement. It appears when the momentum of the ejected electron approximately satisfies the equation $k_e R \sim l\pi$, where R is the molecule's equilibrium distance. This is very similar to the quantization condition for a particle in a box and, therefore, reflects the fact that an integer multiple of half-wavelengths fits within the molecular dimensions. The formula is only expected to work qualitatively at high enough k_e , i.e., when the potential felt by the escaping electron is small compared to its kinetic energy, and it should work better for $\sigma \rightarrow \sigma$ than for $\sigma \rightarrow \pi$ transitions because, in the former, electrons mainly escape along the direction of the molecular axis (see Ref.^{80,154,155} for a more detailed description in the case of the H_2 molecule). The effect is less pronounced in the CO partial wave contributions (see Figs. 10 and 11).

For the $N_2 \sigma_g \rightarrow \sigma_u$ transition (see figure 8), both methods predict that the $l = 3$ partial wave is dominant (~ 1 Mb) in the low energy region (small photoelectron momentum k_e), followed by the $l = 1$ ($\sim 10^{-1} - 10^{-2}$ Mb) and the $l = 5$ ($\sim 10^{-3} - 10^{-4}$ Mb) partial waves. For the $\sigma_u \rightarrow \sigma_g$ transition shown in figure 9a, the situation is slightly different because the $l = 0$ and $l = 2$ partial waves are dominant and comparable in the region of small k_e . For the $\sigma_g \rightarrow \pi_u$ transition (see figure 8b), the $l = 1$ partial wave dominates for $k_e \leq 1$ a.u.. As k_e increases, partial waves with progressively higher l values become dominant: $l = 1$ dominates in the interval $[0, 1.5]$, $l = 3$ in $[1.5, 4.5]$, $l = 5$ in $[4.5, 7]$ and $l = 7$ in $[7, 9]$. This is very similar to what can be observed in Figures 9b for N_2 and Figures 10b and 11b for CO in the case of the $\sigma \rightarrow \pi$ transition. As we will discuss below, the increasing dominant role of higher partial waves is at the origin of coherent two-center electron emission in the case of N_2 and electron diffraction by the neighboring center in the case of CO.

For N_2 and to a lesser extent for CO, the total photoionization cross sections oscillate as functions of photon energy, especially for the $\sigma \rightarrow \sigma$ transitions. For CO, the oscillations are much less pronounced. For N_2 , they have opposite phase in the $1\sigma_g^{-1}$ and $1\sigma_u^{-1}$ channels due to the different bonding character of the orbitals from which the electron is removed. The oscillations are barely visible in a linear scale (notice that we have used logarithmic scale in figures 8, 9, 10 and 11) because they are superimposed to a rapidly decreasing background. The rapid decrease is the consequence of the increasing oscillatory behavior of the continuum wave function with photoelectron energy, which leads to increasing cancellations in the integral given by Equation (3). Oscilla-

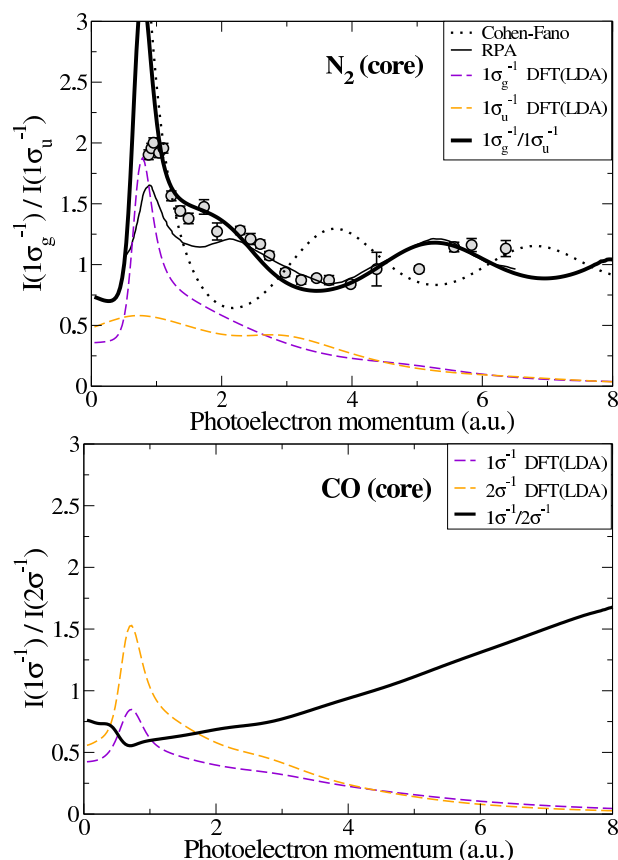


Fig. 12 (Upper panel) Ratio of the $1\sigma_g^{-1}$ and $1\sigma_u^{-1}$ photoionization cross sections of N_2 . DFT calculation: solid line. Experimental data from⁶⁴: open circles. Total cross section (DFT) for $1\sigma_g^{-1}$ and $1\sigma_u^{-1}$ photoionization: dashed lines. (Lower panel) Same as above for the $1\sigma^{-1}$ and $2\sigma^{-1}$ photoionization cross sections of CO.

tions are more clearly visible in the ratio between the corresponding cross sections because the two rapidly decreasing backgrounds compensate each other. The results are shown in Figure 12, where they are compared with experimental data taken from⁶⁴. The agreement between theory and experiment is very good.

The oscillations observed in the N_2 photoionization cross sections as well as in other ionization processes involving homonuclear diatomic molecules^{155–164} are the fingerprint of coherent two-center electron emission. Cohen and Fano gave in 1966⁸² a physical interpretation of these oscillations in the case of H_2 photoionization by assuming that the $1s\sigma_g$ and $1s\sigma_u$ orbitals can be approximately written

$$1s\sigma_{g/u} = \frac{1}{\sqrt{2}}(1s_a \pm 1s_b), \quad (18)$$

where $1s_a$ and $1s_b$ are atomic $1s$ orbitals centered on the a and b protons, respectively, and that the photoionized electron can

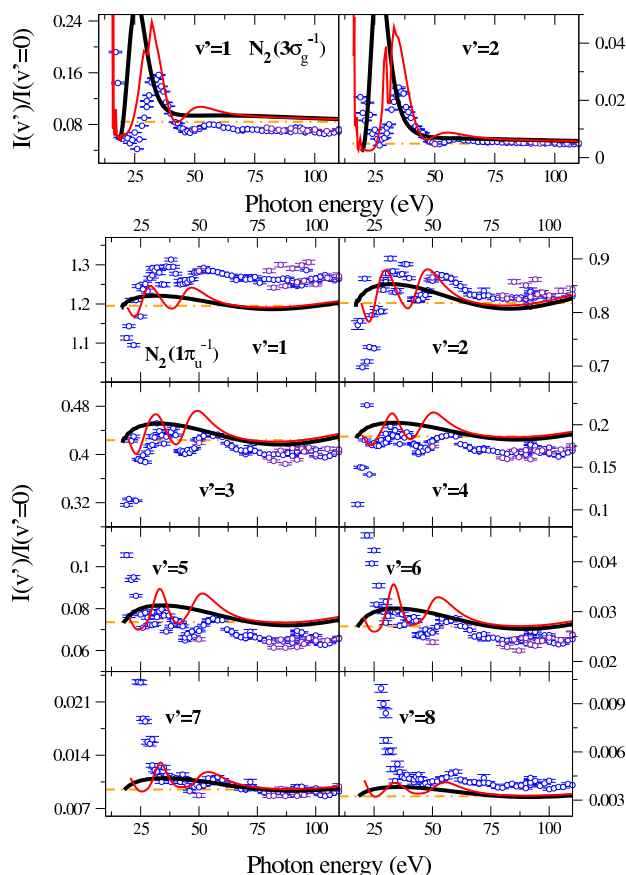


Fig. 13 Ratios of the vibrationally resolved photoionization spectra to the $v' = 0$ cross section as a function of the photon energy for the $3\sigma_g^{-1}$ and $1\pi_u^{-1}$ photoionization of N_2 . Circles: experimental data from⁷⁸ (the different colors indicate different runs). Thick black solid line: DFT method using a LB94 functional (this work). Thin red solid line: TDDFT method using a LB94 functional (this work). Dashed-dotted orange line: Theoretical Franck-Condon value.

be described by a plane wave. Under these assumptions, one obtains

$$\tilde{\sigma}_{g,u}(\omega) = \sigma^{(0)}(\omega) \left(1 \pm \frac{\sin k_e R}{k_e R} \right) \quad (19)$$

where $\sigma^{(0)}$ is a smooth decreasing background, k_e is the photoelectron momentum and R is the equilibrium internuclear distance. This model predicts that the σ_u cross section is exactly shifted by π with respect to the σ_g one, i.e., it oscillates in anti-phase as shown in Figure 12. As mentioned above, due to the rapid decrease of $\tilde{\sigma}$ with photon energy, i.e., with k_e , oscillations are usually hidden. Thus, very often, they must be uncovered by dividing the total cross section by a “reasonable” independent estimate of $\sigma^{(0)}$. This may lead to ambiguous interpretations. Instead, as shown in Figure 12, one can consider the ratio of two rapidly decreasing cross sections as-

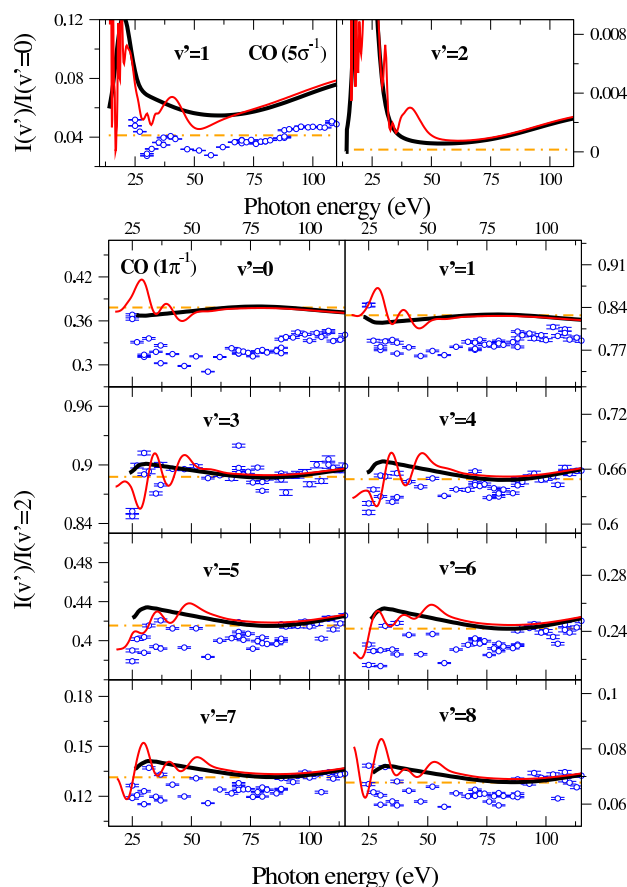


Fig. 14 Same as Fig. 13 for the $5\sigma^{-1}$ and $1\pi^{-1}$ photoionization of CO.

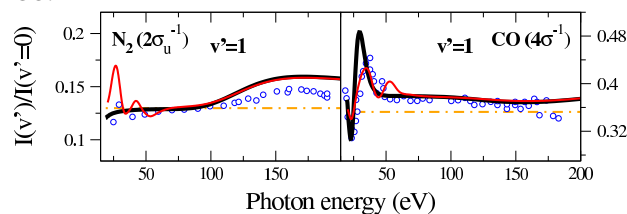


Fig. 15 Ratios of the vibrationally resolved photoionization spectra to the $v' = 0$ cross section as a function of the photon energy for the $2\sigma_g^{-1}$ photoionization of N_2 and the $4\sigma^{-1}$ photoionization of CO. Circles: experimental data from⁵⁸. Thick black solid line: DFT method using a LB94 functional (this work). Thin red solid line: TDDFT method using a LB94 functional (this work). Dashed-dotted orange line: Theoretical Franck-Condon value.

sociated with different ionization channels. Within this model, the ratio between the σ_g and σ_u cross sections is independent of $\sigma^{(0)}$ and is given by:

$$\frac{\tilde{\sigma}_g(\omega)}{\tilde{\sigma}_u(\omega)} \simeq \frac{1 + \Gamma(k_e)}{1 - \Gamma(k_e)} \quad (20)$$

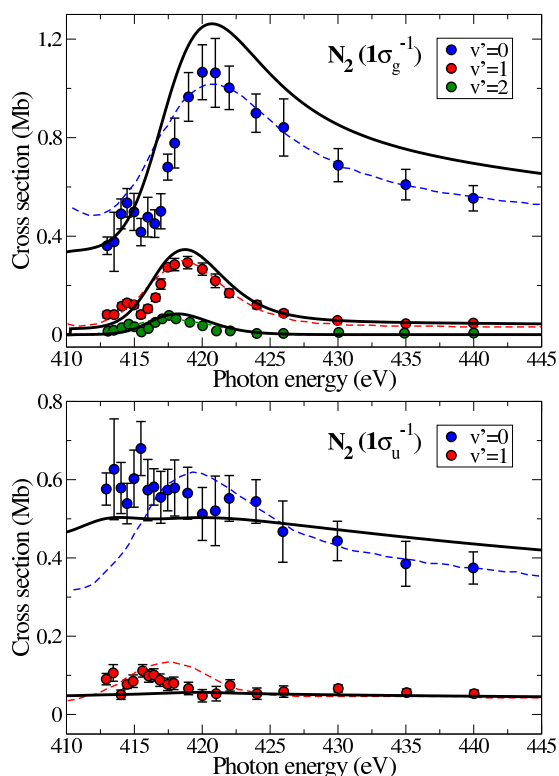


Fig. 16 Vibrationaly resolved cross section for the three first vibrational levels of the $1\sigma_g^{-1}$ and $1\sigma_u^{-1}$ photoionization of N_2 as a function of the photon energy. Circles: experimental data from ⁶³. Thin dashed lines: RPA with the fractional charge basis set RCHF(0.7) from ⁶³. Thick black line: TDDFT method using a LDA functional.

where

$$\Gamma(k_e) = \frac{\sin k_e R}{k_e R} \quad (21)$$

In the case of CO, the lowest molecular orbitals, 1σ and 2σ , are practically identical to the atomic $1s_O$ and $1s_C$ orbitals of oxygen and carbon, respectively. Thus, electrons escape from a well localized area around one of the nuclei. Therefore, coherent two-center emission is not possible and the above oscillatory pattern is not observed in the corresponding $1\sigma/2\sigma$ ratio (see figure 12). Instead, as we will discuss below, another interesting effect may be observed by choosing the appropriate observables: diffraction by the neighboring atomic centers. The latter effect has also been described in previous work ^{104,165}.

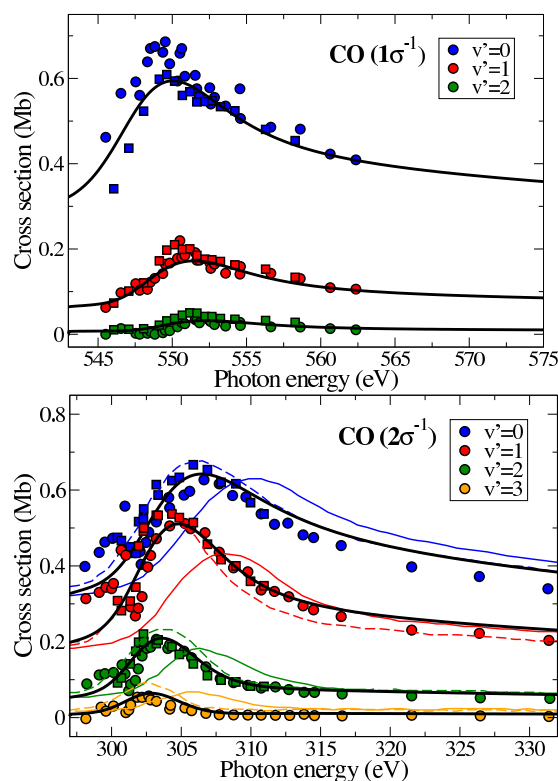


Fig. 17 (Upper panel) Vibrationaly resolved cross section for the three first vibrational levels of the $1\sigma^{-1}$ photoionization of CO as a function of the photon energy. Circles: experimental data from ¹⁴². Squares: experimental data from ⁵⁵. Thick black line: TDDFT method using a LDA functional. (Experimental data were renormalized to the theoretical ones). (Lower panel) Vibrationaly resolved cross section for the four first vibrational levels of the $2\sigma^{-1}$ photoionization of CO as a function of the photon energy. Circles: experimental data from ³⁸. Squares: experimental data from ⁵⁵. Thin solid lines: RCHF with the integer charge $z_e = 1$ from ⁶⁷. Thin dashed lines: RCHF with the fractional charge $z_e = 0.5$ from ⁶⁷. Thick black line: TDDFT method using a LDA functional.

5 Vibrationaly resolved photoionization cross sections

In this section we present vibrationaly-resolved photoionization cross sections for photon energies going from the ionization threshold up to several hundreds eV above it.

5.1 Valence-shell photoionization

Figures 13 and 14 present ratios between vibrationaly resolved photoelectron spectra (v -ratios for short) of N_2 and CO, respectively, calculated by using both the DFT and TD-DFT methods. Only v -ratios associated with ionization from the outer valence orbitals is shown: $3\sigma_g$ and $1\pi_u$ orbitals of N_2 and

5σ and 1π orbitals of CO. The results are compared with very recent experimental data from⁷⁸. For each molecule, the ν -ratios have been extracted by normalizing the vibrationally resolved cross sections to that of the dominant ν -channel. These ratios vary from ~ 1 down to $\sim 10^{-3}$ for the two molecules. The agreement between the results of both theories and the experimental ones is reasonably good, especially for the TD-DFT ones, which reproduce most of the peaks appearing near the ionization threshold. The most important disagreement appears for the very sharp structures lying just above the threshold. There are also some deviations for the largest ν values and photon energies, which is not surprising because the corresponding vibrationally resolved cross sections are very small and, therefore, the measured ν -ratios might be affected by large systematic errors.

The structures observed just above the ionization threshold are due to shape resonances and are correctly described by theory for the largest ν -ratios. The structures appearing at slightly higher photon energies are likely due to interchannel coupling or to resonances associated with singly-excited autoionizing states. As mentioned above, description of these effects is not possible within the DFT approach, but is pretty well achieved within the TD-DFT method.

Figure 15 shows ν -ratios for ionization from the inner valence orbitals. The conclusions are the same as for the outer valence orbitals.

5.2 Core photoionization

In this section we consider photoionization from the $1\sigma_g$ and $1\sigma_u$ orbitals of N_2 , and from the 1σ and 2σ orbitals of CO. Figures 16 and 17 show absolute photoelectron spectra as functions of photon energy for the lowest vibrational states of the remaining molecular cation. Comparison with the available experimental data^{38,55,63,142} is also shown. The comparison is made on absolute scale except for the $1\sigma^{-1}$ cross sections of CO, which were measured in arbitrary units (see the upper panel of Figure 17). In this case, the statistics and the resolution of the experimental data are poorer than in the other three cases.

Good agreement between the present theoretical results, the RPA ones and the experimental data is obtained in most cases. As already noticed when discussing Figures 6 and 8, the $N_2(1\sigma_g^{-1})$ photoelectron spectrum presents a shape resonance at $\omega \sim 420$ eV. The resonance is visible in all the vibrational channels. A similar structure can be seen in the $1\sigma^{-1}$ and $2\sigma^{-1}$ photoelectron spectra of CO (Figure 17). A closer inspection of these figures shows that the position of the resonance peak moves to lower photon energies as ν' increases. The shift between two consecutive ν' components is approximately 2 eV. As has been previously mentioned, the present theoretical results do not predict the existence of pronounced

shape resonances in the $N_2(1\sigma_u^{-1})$ photoelectron spectrum, in good agreement with the experimental data but in disagreement with the RPA spectra that exhibit pronounced maxima similar to those observed in the $N_2(1\sigma_g^{-1})$ case.

Feshbach resonances associated with doubly excited states are probably responsible for the small structures that can be seen in the experimental results shown in Figure 16 at ~ 415 eV (upper panel) and Figure 17 at ~ 300 eV (lower panel). They are less apparent in the $1\sigma_u^{-1}$ photoionization of N_2 (Figure 16, lower panel) probably due to the lower statistics in the experimental data. Their doubly excited nature is confirmed by the fact that neither the present TD-DFT results nor the RPA ones predict the existence of these structures.

5.3 Valence-shell and core photoionization at high photon energies

Figures 18, 19 and 20 present experimental and calculated ν -ratios as functions of photon energy for the valence-shell ionization processes $N_2 \rightarrow N_2^+(3\sigma_g^{-1}, \nu')$ and $N_2 \rightarrow N_2^+(1\pi_u^{-1}, \nu')$, $CO \rightarrow CO^+(5\sigma^{-1}, \nu')$ and $CO \rightarrow CO^+(1\pi^{-1}, \nu')$, and $N_2 \rightarrow N_2^+(2\sigma_u^{-1}, \nu')$ and $CO \rightarrow CO^+(4\sigma^{-1}, \nu')$, respectively. Good agreement between theory and experiment is observed except for the higher ν' values and the largest photon energies, for which the vibrationally resolved cross sections are very small.

A common feature to all the ν -ratios is the presence of pronounced oscillations around the value predicted by the Franck-Condon (FC) approximation. These oscillations are less visible for CO than for N_2 . As shown in Ref.⁷⁸, they can also be explained as resulting from coherent two-center electron emission. Indeed, by generalizing Cohen-Fano ideas to the case of vibrationally resolved photoelectron spectra for both homonuclear and heteronuclear diatomic molecules, one can approximately write⁷⁸

$$\sigma_0 \left| \int_0^\infty \chi_{\nu_0}(R) \left[1 + 2c_A c_B \frac{\sin(k_{e,\nu'} R)}{k_{e,\nu'} R} \right]^{\frac{1}{2}} \chi_{\nu'}(R) dR \right|^2, \quad (22)$$

where c_A and c_B are the mixing coefficients of the atomic orbitals ϕ_A and ϕ_B in the molecular orbital ψ

$$\psi = c_A \phi_A + c_B \phi_B \quad (23)$$

and $c_A^2 + c_B^2 = 1$. For the valence orbitals of N_2 , $|c_A| = |c_B|$ due to the inversion symmetry of the molecule, while for the valence orbitals of CO, these coefficients are different.

A reasonable choice for CO is $c_A^2 = 0.32$ and $c_B^2 = 0.68$, which correspond to the normalized electron occupancy of the C and O valence orbitals, respectively, resulting from a simple Hartree-Fock calculation performed with a minimal basis of

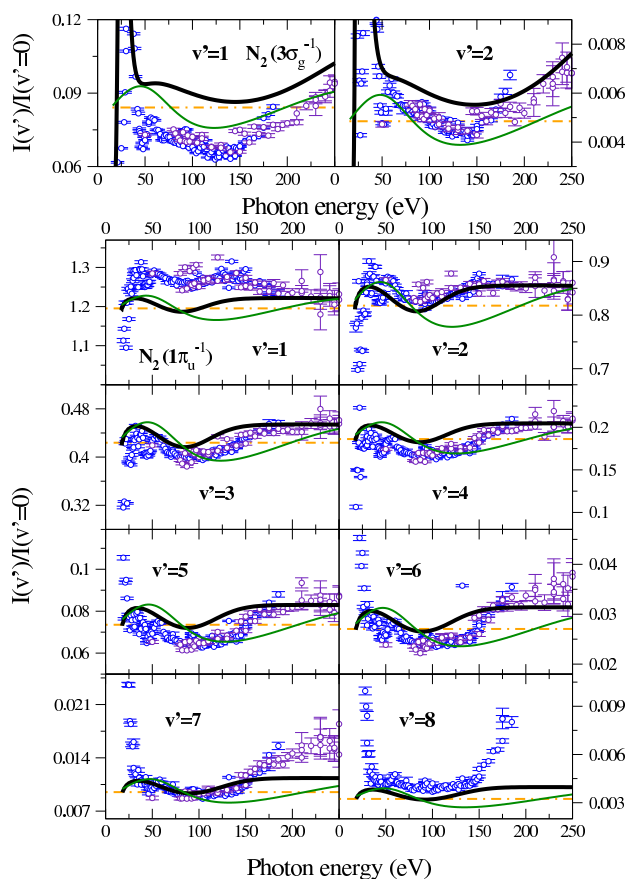


Fig. 18 Ratios of the vibrationally resolved photoionization spectra to the $v' = 0$ cross section as a function of the photon energy for the $3\sigma_g^{-1}$ and $1\pi_u^{-1}$ photoionization of N_2 . Circles: experimental data from⁷⁸ (the different colors indicate different runs). Thick black solid line: DFT method using a LB94 functional (this work). Thin green solid line: vibrationally resolved Cohen-Fano results obtained from equation (22) (this work). Dashed-dotted orange line: Theoretical Franck-Condon value.

atomic orbitals. Photoelectron spectra corresponding to different final v' states of the remaining molecular cation probe different regions of R . Thus one can simplify equation (22) by replacing the variable R by the characteristic value $R_{v'}$ associated with the v' vibrational state, then performing a first-order expansion of $I(v'_b)/I(v'_a)$ in terms of $\delta R_{v'_b} = R_{v'_b} - R_{v'_a}$, and finally taking the limit to large values of the electron momentum k_e . Hence one obtains

$$\frac{I(v'_b)}{I(v'_a)} = \frac{|\langle \chi_{v'_b} | \chi_{v'_a} \rangle|^2}{|\langle \chi_{v'_b} | \chi_{v'_a} \rangle|^2} \left[1 + 2c_{ACB} \frac{\delta R_{v'_b}}{R_{v'_a}} \cos(k_e R_{v'_a}) \right]. \quad (24)$$

The formula predicts that the $I(v'_b)/I(v'_a)$ ratio should approximately oscillate around the Franck-Condon value $|\langle \chi_{v'_b} | \chi_{v'_a} \rangle|^2 / |\langle \chi_{v'_b} | \chi_{v'_a} \rangle|^2$ with a $\cos(k_e R_{v'_a})$ dependence

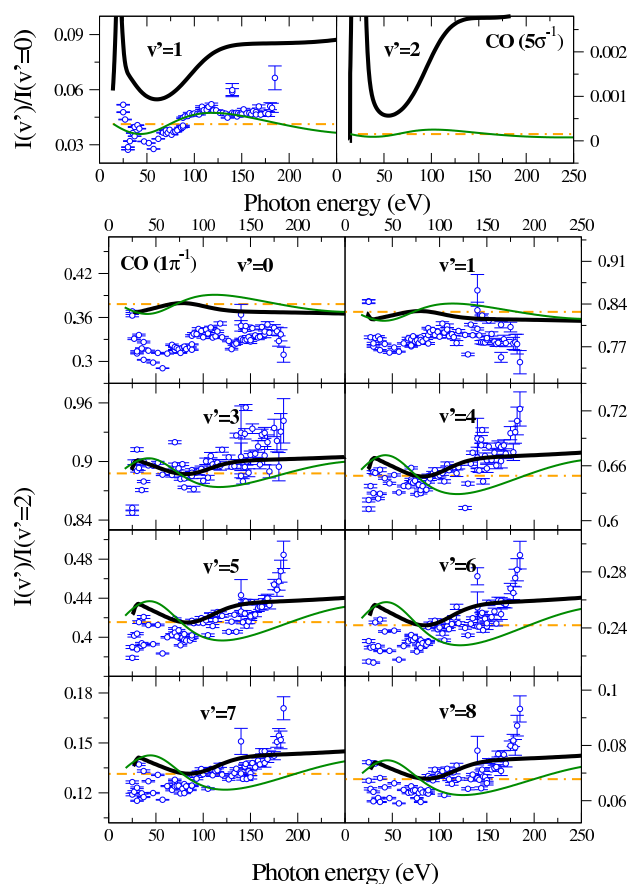


Fig. 19 Same as Fig. 18 for the $5\sigma^{-1}$ and $1\pi^{-1}$ photoionization of CO.

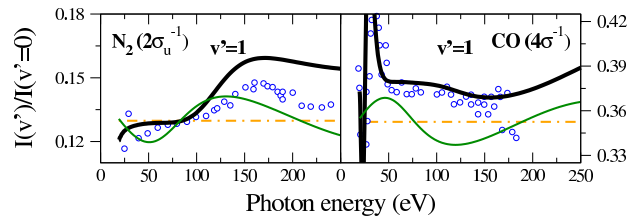


Fig. 20 Ratios of the vibrationally resolved photoionization spectra to the $v' = 0$ cross section as a function of the photon energy for the $2\sigma_u^{-1}$ photoionization of N_2 and the $4\sigma^{-1}$ photoionization of CO. Circles: experimental data from⁵⁸. Thick black solid line: DFT method using a LB94 functional (this work). Thin green solid line: vibrational Cohen-Fano calculations (this work). Dashed-dotted orange line: Theoretical Franck-Condon value.

and amplitude proportional to $\delta R_{v'_b}/R_{v'_a}$. This is precisely the qualitative behavior observed in all the ratios depicted in figures 18, 19 and 20. Notice that, when $R_{v'_b}$ is smaller than $R_{v'_a}$, the ratio $\delta R_{v'_b}/R_{v'_a}$ is negative and, therefore, the oscillations have opposite phase. This can be clearly seen in figure 19, when comparing the $v' = 0/v' = 2$ and $v' = 1/v' = 2$ ratios

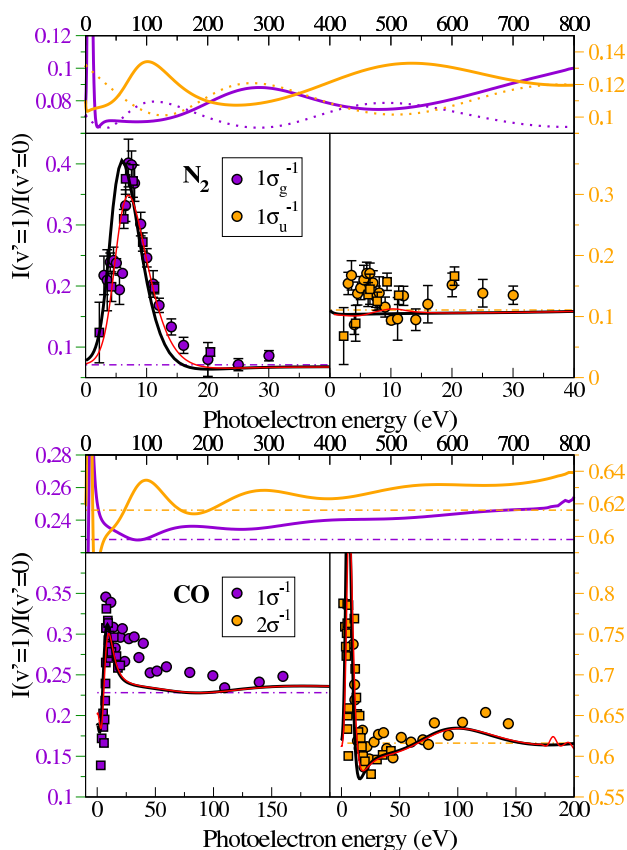


Fig. 21 (Upper panel) $v' = 1/v' = 0$ cross section ratios for the $1\sigma_g^{-1}$ and $1\sigma_u^{-1}$ photoionization of N_2 as a function of the photoelectron energy (upper panel: large range; lower panels: small range). Circles: experimental data from⁶³. Squares: experimental data from⁶². Thick black and colored lines: DFT method using a LDA functional. Red thin lines: TDDFT method using a LDA functional. Dotted lines: vibrational Cohen-Fano calculations (see⁷⁸). (Lower panel) $v' = 1/v' = 0$ cross section ratios for the $1\sigma^{-1}$ and $2\sigma^{-1}$ photoionization of CO as a function of the photoelectron energy (upper panel: large range; lower panels: small range). Circles: experimental data from⁵⁶. Squares: experimental data from Kugeler et al. published in⁵⁶. Thick black and colored lines: DFT method using a LDA functional. Red thin lines: TDDFT method using a LDA functional. Dashed-dotted lines: theoretical Franck-Condon values.

with the $v' = 3/v' = 2$, $v' = 4/v' = 2$, etc, ones.

Figure 21 presents experimental and calculated v -ratios as functions of photon energy for the core ionization processes $N_2 \rightarrow N_2(1\sigma_g^{-1})$ and $N_2 \rightarrow N_2(1\sigma_u^{-1})$ (upper panel), and $CO \rightarrow CO^+(1\sigma^{-1}, v')$ and $CO \rightarrow CO^+(2\sigma^{-1}, v')$ (lower panel). As in valence-shell photoionization, oscillations are quite apparent. In the upper panel of Figure 21, one can see that the model describes pretty well the oscillations in the v -ratios for both the $N_2(1\sigma_g^{-1})$ and $N_2(1\sigma_u^{-1})$ channels.

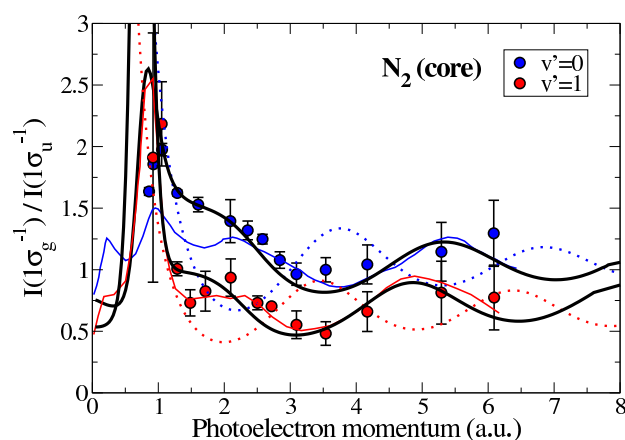


Fig. 22 σ_g/σ_u cross section ratios for the $1\sigma_g^{-1}$ and $1\sigma_u^{-1}$ photoionization of N_2 as a function of the photoelectron momentum. Circles: experimental data from⁶⁴. Thin blue and red lines: RPA calculations from⁶⁴. Thick black lines: DFT method using a LDA functional. Dotted lines: vibrational Cohen-Fano calculations (see⁷⁸).

A blow up of the low energy region, also shows a very good agreement with the available experimental data. In the case of CO (lower panel of figure 21), oscillations are also quite apparent, also in the experimental data, but they cannot be explained by the model because the core 1σ and 2σ orbitals of CO are localized on the atomic centers, i.e., either c_A or c_B is zero in equation (23), and, consequently, the interference term in equations (22) and (24) vanishes. In this case, as already anticipated in section 4.3, the origin of the oscillations is diffraction of the electron ejected from one of the atomic centers by the other atomic center.

These results clearly illustrate that, by determining v -ratios, one can easily circumvent the problem of identifying two-center interferences and diffraction in the individual vibrationally resolved photoelectron spectra, in which such effects would be barely visible due to the rapid decrease of the corresponding cross sections with photon energy. As explained in section 4.3, another way to visualize these interferences is to plot the ratio between non vibrationally resolved photoelectron spectra corresponding to ionization from different molecular orbitals, e.g., the $1\sigma_g$ and $1\sigma_u$ orbitals in N_2 (see figure 12). Figure 22 shows that similar oscillations appear in the ratios between vibrationally resolved $N_2(1\sigma_g^{-1})$ and $N_2(1\sigma_u^{-1})$ photoelectron spectra. As can be seen, oscillations are quite apparent for the individual final vibrational states of the molecular cation. The agreement between the present theoretical results and experiment is excellent. Earlier RPA results also agree, but they provide a poorer description at low photon energies. The figure also shows that our extension of the Cohen-Fano model described above predicts oscillations

with a similar period, but they are out of phase. This is because, as a result of the many approximations made to obtain equation (22), the model does not account for the relative phase between the $N_2(1s\sigma_g^{-1})$ and $N_2(1s\sigma_u^{-1})$ channels.

6 Conclusions

We have presented a detailed description of theoretical methods based on density functional theory specially designed to obtain vibrationally resolved photoionization cross sections of simple molecules within the Born-Oppenheimer approximation. The methods have been successfully applied to N_2 and CO in a wide range of photon energies. At high photon energies, static-exchange-DFT and TDDFT lead to almost identical results in good agreement with experiment for both vibrationally and non-vibrationally resolved photoelectron spectra, while, at low photon energies, TDDFT is able to describe features observed near the ionization threshold but not arising from static-exchange-DFT, such as singly-excited Feshbach resonances and structures resulting from interchannel coupling. TDDFT also provides a better description of shape resonances. Very often, this description is of similar quality as that obtained from more elaborate multireference or close coupling methods, which are prohibitively expensive to obtain vibrationally resolved photoelectron spectra in complex molecules. It is also a bit more accurate than that provided by RPA methods, whose computational cost is similar but whose accuracy often relies on the introduction of fitting parameters. Therefore, DFT-like methods as those presented in this manuscript are a promising tool to evaluate vibrationally resolved photoelectron spectra in more complex molecules, as recent applications have shown for CH_4 ¹²⁵ and C_2H_2 ¹²⁴.

We have paid a particular attention to the region of high photon energies, where the electron wavelength is comparable to the bond length and, therefore, two-center interferences and diffraction are expected to occur. In this region, the main experimental difficulty is to extract the relatively small interference and diffraction features from the rapidly decreasing cross section as a function of photon energy. However, this difficulty can be easily overcome by determining ratios of vibrationally resolved photoelectron spectra. For both N_2 and CO, these ratios exhibit pronounced oscillations that, in the case of valence shell photoionization, are mainly due to the coherent emission of electrons from the two atomic centers⁷⁸ and, in the case of K-shell photoionization, are due either to a similar effect as for N_2 or to diffraction of the ejected electron by the neighboring atomic center as for CO. These structures can thus provide direct information about the molecular geometry.

Effects that cannot be described with these DFT-like methods are resonances associated with double or multiple excitations. Also, although in principle TDDFT is able to describe

Feshbach resonances associated with singly excited states as it does for instance in atoms, it may fail in the molecular case due to the use of the Born-Oppenheimer approximation. Indeed, in many cases, the autoionization lifetimes of these resonances are comparable or even larger than the time employed by the nuclei to move significantly. Under these circumstances, the use of the Born-Oppenheimer approximation is not justified and consequently may lead to wrong results. This is the case, e.g., for the autoionization decay of H_2 ¹⁴⁹, for which an accurate description of the experimental findings in the region of the autoionizing states requires going beyond the Born-Oppenheimer approximation. Future theoretical developments should focus on solving these problems in order to improve the performance of DFT-like methods because these are so far the only ones able to provide vibrationally resolved cross sections all the way from diatomics to large, symmetric molecules.

Acknowledgments

We thank Mare Nostrum BSC, Cineca and CCC-UAM for allocation of computer time. Work supported by the MICINN project Nos. FIS2010-15127, ACI2008-0777 and CSD 2007-00010 (Spain), the ERA-Chemistry project PIM2010EEC-00751, the European COST Action CM0702, the Marie Curie ITN CORINF (EU), and the XCHEM Advanced Grant 290853 of the European Research Council.

References

- 1 J. W. Gallagher, C. E. Brion, J. A. R. Samson and P. W. Langhoff, *J. Phys. Chem. Ref. Data*, 1988, **17**, 9–153.
- 2 R. B. Kay, P. E. Van der Leeuw and M. J. Van der Wiel, *J. Phys. B: At. Mol. Opt. Phys.*, 1977, **10**, 2513–2519.
- 3 N. A. Cherepkov, S. K. Semenov, Y. Hikosaka, K. Ito, S. Motoki and A. Yagishita, *Phys. Rev. Lett.*, 2000, **84**, 250–253.
- 4 X.-J. Liu, G. Prümper, F. Gel'mukhanov, N. A. Cherepkov, H. Tanaka and K. Ueda, *J. Electron Spectrosc. Relat. Phenom.*, 2007, **156–158**, 73–77.
- 5 E. W. Plummer, T. Gustafsson, W. Gudat and D. E. Eastman, *Phys. Rev. A*, 1977, **15**, 2339–2355.
- 6 A. Hamnett, W. Stoll and C. E. Brion, *J. Electron Spectrosc. Relat. Phenom.*, 1976, **8**, 367–376.
- 7 P. R. Woodruff and G. V. Marr, *Proc. R. Soc. Lond. A*, 1977, **358**, 87–103.
- 8 J. A. R. Samson, G. N. Haddad and J. L. Gardner, *J. Phys. B: At. Mol. Opt. Phys.*, 1977, **10**, 1749–1759.
- 9 S. K. Semenov and N. A. Cherepkov, *Phys. Rev. A*, 2002, **66**, 022708.
- 10 T. N. Rescigno and P. W. Langhoff, *Chem. Phys. Lett.*, 1977, **51**, 65–70.
- 11 J. L. Dehmer and D. Dill, *J. Chem. Phys.*, 1976, **65**, 5327.
- 12 I. Wilhelmy and N. Rösch, *Chem. Phys.*, 1994, **185**, 317–332.
- 13 N. A. Cherepkov and S. K. Semenov, *Int. J. Quantum Chem.*, 2007, **107**, 2889–2901.
- 14 D. L. Lynch and V. McKoy, *Phys. Rev. A*, 1984, **30**, 1561–1564.
- 15 J. L. Dehmer and D. Dill, *Phys. Rev. Lett.*, 1975, **35**, 213–215.
- 16 P. Lin and R. R. Lucchese, *J. Synchrotron Radiat.*, 2001, **8**, 150–153.

- 17 M. Stener, G. Fronzoni and P. Decleva, *Chem. Phys. Lett.*, 2002, **351**, 469–474.
- 18 P. Lin and R. R. Lucchese, *J. Chem. Phys.*, 2002, **117**, 4348.
- 19 J. Schirmer and F. Mertins, *J. Phys. B: At. Mol. Opt. Phys.*, 1996, **29**, 3559–3580.
- 20 M. Tashiro, *J. Chem. Phys.*, 2010, **132**, 134306–1.
- 21 M. Tashiro, M. Ehara, H. Fukuzawa, K. Ueda, C. Buth, N. V. Kryzhevoi and L. S. Cederbaum, *J. Chem. Phys.*, 2010, **132**, 134306.
- 22 R. R. Lucchese and R. W. Zurales, *Phys. Rev. A*, 1991, **44**, 291.
- 23 S. Yabushita, C. W. McCurdy and T. N. Rescigno, *Phys. Rev. A*, 1987, **36**, 3146–3151.
- 24 M. Stener, G. De Alti and P. Decleva, *Theor. Chem. Acc.*, 1999, **101**, 247–256.
- 25 R. E. Stratmann, G. Bandarage and R. R. Lucchese, *Phys. Rev. A*, 1995, **51**, 3756.
- 26 I. Cacelli, R. Moccia and A. Rizzo, *Phys. Rev. A*, 1998, **57**, 1895–1905.
- 27 S. K. Semenov, N. A. Cherepkov, G. Fecher and G. Schönhense, *Phys. Rev. A*, 2000, **61**, 032704.
- 28 L. Veseth, *J. Phys. B: At. Mol. Opt. Phys.*, 1994, **27**, 481–496.
- 29 L. A. Collins and B. I. Schneider, *Phys. Rev. A*, 1984, **29**, 1695.
- 30 G. Raev, H. Le Rouzo and H. Lefebvre-Brion, *J. Chem. Phys.*, 1980, **72**, 5701.
- 31 R. Montuoro and R. Moccia, *Chem. Phys.*, 2003, **293**, 281–308.
- 32 R. R. Lucchese, G. Raev and V. McKoy, *Phys. Rev. A*, 1982, **25**, 2572–2587.
- 33 M. Stener and P. Decleva, *J. Chem. Phys.*, 2000, **112**, 10871.
- 34 J. W. Davenport, *Phys. Rev. Lett.*, 1976, **36**, 945–949.
- 35 B. Basden and R. R. Lucchese, *Phys. Rev. A*, 1988, **37**, 89.
- 36 C. M. Truesdale, D. W. Lindle, P. H. Kobrin, U. Becker, H. G. Kerkhoff, P. A. Heimann, T. A. Ferrett and D. A. Shirley, *J. Chem. Phys.*, 1984, **80**, 2319.
- 37 A. P. Hitchcock, P. Lablanquie, P. Morin, E. Lizon, A. Lugrin, M. Simon, P. Thiry and I. Nenner, *Phys. Rev. A*, 1988, **37**, 2448.
- 38 H. M. Köppe, A. L. D. Kilcoyne, J. Feldhaus and A. M. Bradshaw, *J. Electron Spectrosc. Relat. Phenom.*, 1995, **75**, 97–108.
- 39 J. E. Hardis, T. A. Ferrett, S. H. Southworth, A. C. Parr, P. Roy, J. L. Dehmer, P. M. Dehmer and W. A. Chupka, *J. Chem. Phys.*, 1988, **89**, 812.
- 40 J. A. R. Samson and J. L. Gardner, *J. Electron Spectrosc. Relat. Phenom.*, 1976, **8**, 35–44.
- 41 M. R. F. Siggel, M. A. Hayes, M. A. MacDonald, J. B. West, J. L. Dehmer, A. C. Parr, J. E. Hardis, I. Iga and V. Tiit, *J. Chem. Phys.*, 1992, **96**, 7433.
- 42 J. Schirmer, M. Braunstein and V. McKoy, *Phys. Rev. A*, 1990, **41**, 283.
- 43 N. A. Cherepkov, S. K. Semenov, A. V. Golovin, J.-i. Adachi and A. Yagishita, *J. Phys. B: At. Mol. Opt. Phys.*, 2004, **37**, 4803–4815.
- 44 S. K. Semenov, N. A. Cherepkov, A. De Fanis, Y. Tamenori, M. Kitajima, H. Tanaka and K. Ueda, *J. Electron Spectrosc. Relat. Phenom.*, 2005, **144–147**, 211–214.
- 45 A. M. Velasco, I. Martín and C. Lavín, *Int. J. Quantum Chem.*, 2005, **104**, 517–521.
- 46 R. R. Lucchese and V. McKoy, *Phys. Rev. A*, 1983, **28**, 1382.
- 47 N. Padial, G. Csanak, V. McKoy and P. W. Langhoff, *J. Chem. Phys.*, 1978, **69**, 2992.
- 48 M. E. Smith, D. L. Lynch and V. McKoy, *J. Chem. Phys.*, 1986, **85**, 6455–6459.
- 49 M. Stener, P. Decleva, I. Cacelli, R. Moccia and R. Montuoro, *Chem. Phys.*, 2001, **272**, 15–25.
- 50 J.-i. Adachi, K. Hosaka, S. Furuya, K. Soejima, M. Takahashi, A. Yagishita, S. K. Semenov and N. A. Cherepkov, *J. Electron Spectrosc. Relat. Phenom.*, 2004, **137–140**, 243–248.
- 51 H. M. Köppe, B. Kempgens, A. L. D. Kilcoyne, J. Feldhaus and A. M. Bradshaw, *Chem. Phys. Lett.*, 1996, **260**, 223–228.
- 52 S. K. Semenov, N. A. Cherepkov, A. De Fanis, Y. Tamenori, M. Kitajima, H. Tanaka and K. Ueda, *Phys. Rev. A*, 2004, **70**, 052504.
- 53 K. J. Randall, A. L. D. Kilcoyne, H. M. Köppe, J. Feldhaus, A. M. Bradshaw, J.-E. Rubensson, W. Eberhardt, Z. Xu, P. D. Johnson and Y. Ma, *Phys. Rev. Lett.*, 1993, **71**, 1156–1159.
- 54 J.-i. Adachi, K. Hosaka, S. Furuya, K. Soejima, M. Takahashi, A. Yagishita, S. K. Semenov and N. A. Cherepkov, *Phys. Rev. Lett.*, 2003, **91**, 163001.
- 55 D. A. Mistrov, A. De Fanis, M. Kitajima, M. Hoshino, H. Shindo, T. Tanaka, Y. Tamenori, H. Tanaka, A. A. Pavlychev and K. Ueda, *Phys. Rev. A*, 2003, **68**, 022508.
- 56 M. Matsumoto, K. Ueda, E. Kukk, H. Yoshida, T. Tanaka, M. Kitajima, H. Tanaka, Y. Tamenori, K. Kuramoto, M. Ehara and H. Nakatsuji, *Chem. Phys. Lett.*, 2006, **417**, 89–93.
- 57 R. Stockbauer, B. E. Cole and D. L. Ederer, *Phys. Rev. Lett.*, 1979, **43**, 757.
- 58 G. J. Rathbone, R. M. Rao, E. D. Poliakov, K. Wang and V. McKoy, *J. Chem. Phys.*, 2004, **120**, 778–780.
- 59 B. Kempgens, A. Kivimäki, M. Neeb, H. M. Köppe, A. M. Bradshaw and J. Feldhaus, *J. Phys. B: At. Mol. Opt. Phys.*, 1996, **29**, 5389–5402.
- 60 K. Ueda, R. Püttner, N. A. Cherepkov, F. Gel'mukhanov and M. Ehara, *Eur. Phys. J. Special Topics*, 2009, **169**, 95–107.
- 61 S. K. Semenov, N. A. Cherepkov, M. Matsumoto, T. Hatamoto, X.-J. Liu, G. Prümper, T. Tanaka, M. Hoashino, H. Tanaka, F. Gel'mukhanov and K. Ueda, *J. Phys. B: At. Mol. Opt. Phys.*, 2006, **39**, L261–L267.
- 62 U. Hergenhahn, O. Kugeler, A. Rüdell, E. E. Rennie and A. M. Bradshaw, *J. Phys. Chem. A*, 2001, **105**, 5704–5708.
- 63 S. K. Semenov, N. A. Cherepkov, M. Matsumoto, K. Fujiwara, K. Ueda, E. Kukk, F. Tahara, T. Sunami, H. Yoshida, T. Tanaka, K. Nakagawa, M. Kitajima, H. Tanaka and A. De Fanis, *J. Phys. B: At. Mol. Opt. Phys.*, 2006, **39**, 375–386.
- 64 X.-J. Liu, N. A. Cherepkov, S. K. Semenov, V. Kimberg, F. Gel'mukhanov, G. Prümper, T. Lischke, T. Tanaka, M. Hoshino, H. Tanaka and K. Ueda, *J. Phys. B: At. Mol. Opt. Phys.*, 2006, **39**, 4801–4817.
- 65 A. A. Pavlychev, *J. Phys. B: At. Mol. Opt. Phys.*, 1999, **32**, 2077–2088.
- 66 A. A. Pavlychev and D. A. Mistrov, *J. Phys. B: At. Mol. Opt. Phys.*, 2009, **42**, 055103.
- 67 S. K. Semenov, N. A. Cherepkov, T. Jahnke and R. Dörner, *J. Phys. B: At. Mol. Opt. Phys.*, 2004, **37**, 1331–1342.
- 68 B. Leyh and G. Raev, *Phys. Rev. A*, 1986, **34**, 2920.
- 69 K. Ueda, X.-J. Liu, G. Prümper, T. Lischke, T. Tanaka, M. Hoshino, H. Tanaka, I. Minkov, V. Kimberg and F. Gel'mukhanov, *Chem. Phys.*, 2006, **329**, 329–337.
- 70 K. Ueda, *J. Phys.: Conf. Ser.*, 2010, **212**, 012033.
- 71 F. Gel'mukhanov, V. Kimberg, X.-J. Liu, G. Prümper, T. Tanaka, M. Hoshino, H. Tanaka and K. Ueda, *J. Electron Spectrosc. Relat. Phenom.*, 2007, **156–158**, 265–269.
- 72 E. D. Poliakov and R. R. Lucchese, *Phys. Scripta*, 2006, **74**, C71.
- 73 R. R. Lucchese, J. D. Bozek, A. Das and E. D. Poliakov, *J. Chem. Phys.*, 2009, **131**, 044311.
- 74 R. Das, C. Wu, A. G. Mihill, E. D. Poliakov, K. Wang and V. McKoy, *J. Phys. Chem.*, 1995, **99**, 1741–1747.
- 75 E. D. Poliakov, H. C. Choi, R. M. Rao, A. G. Mihill, S. Kakar, K. Wang and V. McKoy, *J. Chem. Phys.*, 1995, **103**, 1773–1787.
- 76 K. Hosaka, J.-i. Adachi, A. V. Golovin, M. Takahashi, T. Teramoto, N. Watanabe, T. Jahnke, T. Weber, M. S. Schöffler, L. P. H. Schmidt, T. Osipov, O. Jagutzki, A. L. Landers, M. H. Prior, H. Schmidt-Böcking, R. Dörner, A. Yagishita, S. K. Semenov and N. A. Cherepkov, *Phys. Rev. A*, 2006, **73**, 022716.
- 77 T. D. Thomas, E. Kukk, T. Ouchi, A. Yamada, H. Fukuzawa, K. Ueda, R. Püttner, I. Higuchi, Y. Tamenori, T. Asahina, N. Kuze, H. Kato,

- M. Hoshino, H. Tanaka, A. Lindblad and L. J. Sæthre, *J. Chem. Phys.*, 2010, **133**, 174312.
- 78 S. E. Canton, E. Plésiat, J. D. Bozek, B. S. Rude, P. Decleva and F. Martín, *Proc. Natl. Acad. Sci.*, 2011, **108**, 7302–7306.
- 79 C. J. Davisson, *Nobel Lecture*, 1937, 387.
- 80 J. Fernández, O. Fojón, A. Palacios and F. Martín, *Phys. Rev. Lett.*, 2007, **98**, 043005.
- 81 U. Becker, *Nature*, 2011, **474**, 586.
- 82 H. D. Cohen and U. Fano, *Phys. Rev.*, 1966, **150**, 30–33.
- 83 H. J. Wörner, J. B. Bertrand, D. V. Kartashov, P. B. Corkum and D. M. Villeneuve, *Nature*, 2010, **466**, 604.
- 84 F. Krasniqi, B. Najjari, L. Struder, D. Rolles, A. Voitkiv, and J. Ullrich, *Phys. Rev. A*, 2010, **81**, 033411.
- 85 C. Altucci, R. Velotta and J. P. Marangos, *J. Mod. Opt.*, 2010, **57**, 916.
- 86 P. J. Benning, D. M. Poirier, N. Troullier, J. L. Martins, J. H. Weaver, R. E. Haufler, L. P. F. Chibante and R. E. Smalley, *Phys. Rev. B*, 1991, **44**, 1962.
- 87 T. Liebsch, O. Plotzke, F. Heiser, U. Hergenbahn, O. Hemmers, R. Wehlitz, J. Viefhaus, B. Langer, S. B. Whitfield and U. Becker, *Phys. Rev. A*, 1995, **52**, 457.
- 88 P. Colavita, G. D. Alti, G. Fronzoni, M. Stener and P. Decleva, *Phys. Chem. Chem. Phys.*, 2001, **3**, 4481.
- 89 P. Decleva, S. Furlan, G. Fronzoni and M. Stener, *Chem. Phys. Lett.*, 2001, **384**, 363.
- 90 O. Frank and J. M. Rost, *Chem. Phys. Lett.*, 1997, **271**, 367.
- 91 Y. B. Xu, M. Q. Tan and U. Becker, *Phys. Rev. Lett.*, 1996, **76**, 3538.
- 92 T. Liebsch, R. Hentges, A. Rüdél, J. Viefhaus, U. Becker and R. Schlögl, *Chem. Phys. Lett.*, 1997, **279**, 197.
- 93 S. Korica, A. Reinköster, M. Braune, J. Viefhaus, D. Rolles, B. Langer, G. Fronzoni, D. Toffoli, M. Stener, P. Decleva, O. M. Al-Dossary and U. Becker, *Surf. Sci.*, 2010, **604**, 1940.
- 94 Y.-J. Lia, P. Wanga, J.-F. Nia, L. Menga, X.-B. Wanga, C.-Q. Shenga, H.-N. Lia, W.-H. Zhangb, Y. Xub, F.-Q. Xub and J.-F. Zhu, *J. Electron Spectrosc. Relat. Phenom.*, 2011, **184**, 414.
- 95 J. Viefhaus and M. Illchen, private communication.
- 96 D. Toffoli and P. Decleva, *Phys. Rev. A*, 2010, **81**, 061201(R).
- 97 J. Rehr, W. Schattke, F. J. García de Abajo, R. Díez Muño and M. A. Van Hove, *J. Electron Spectrosc. Relat. Phenom.*, 2002, **126**, 67–76.
- 98 R. Díez Muño, D. Rolles, F. J. García de Abajo, C. S. Fadley and M. A. Van Hove, *Surf. Rev. Lett.*, 2002, **9**, 1213–1217.
- 99 D. L. Foulis, R. F. Petitfer and P. Sherwood, *Europhys. Lett.*, 1995, **29**, 647.
- 100 M. Y. Amusia and A. S. Baltenkov, *Cent. Eur. J. Phys.*, 2010, **8**, 825–832.
- 101 P. W. Langhoff, S. R. Langhoff, T. N. Rescigno, J. Schirmer, L. S. Cederbaum, W. Domcke and W. von Niessen, *Chem. Phys.*, 1981, **58**, 71–91.
- 102 C. Winstead and P. W. Langhoff, *J. Chem. Phys.*, 1991, **95**, 3107–3118.
- 103 B. Zimmermann, K. Wang and V. McKoy, *Phys. Rev. A*, 2003, **67**, 042711.
- 104 B. Zimmermann, D. Rolles, B. Langer, R. Hentges, M. Braune, S. Cvejanović, O. Geßner, F. Heiser, S. Korica, T. Lischke, A. Reinköster, J. Viefhaus, R. Dörner, V. McKoy and U. Becker, *Nature Physics*, 2008, **4**, 649–655.
- 105 D. Rolles, M. Braune, S. Cvejanović, O. Gessner, R. Hentges, S. Korica, B. Langer, T. Lischke, G. Prümper, A. Reinköster, J. Viefhaus, B. Zimmermann, V. McKoy and U. Becker, *Nature*, 2005, **437**, 711–715.
- 106 D. L. Lynch, *Phys. Rev. A*, 1991, **43**, 5176.
- 107 D. Toffoli, M. Stener, G. Fronzoni and P. Decleva, *Chem. Phys.*, 2002, **276**, 25–43.
- 108 I. Wilhelmy, L. Ackermann, A. Görling and N. Rösch, *J. Chem. Phys.*, 1994, **100**, 2808.
- 109 G. Bandarage and R. R. Lucchese, *Phys. Rev. A*, 1993, **47**, 1989.
- 110 J. Tennyson, *Phys. Rep.*, 2010, **491**, 29.
- 111 P. V. Demekhin, A. Ehresmann and V. L. Sukhorukov, *J. Chem. Phys.*, 2011, **134**, 024113.
- 112 T. Jahnke, T. Weber, A. L. Landers, A. Knapp, S. Schössler, J. Nickles, S. Kammer, O. Jagutzki, L. P. H. Schmidt, A. Czasch, T. Osipov, E. Arenholz, A. Young, R. Díez Muño, D. Rolles, F. J. García de Abajo, C. S. Fadley, M. A. Van Hove, S. K. Semenov, N. A. Cherepkov, J. Rösch, M. H. Prior, H. Schmidt-Böcking, C. L. Cocke and R. Dörner, *Phys. Rev. Lett.*, 2002, **88**, 073002.
- 113 M. S. Schöffler, J. Titze, N. Petridis, T. Jahnke, K. Cole, L. P. H. Schmidt, A. Czasch, D. Akoury, O. Jagutzki, J. B. Williams, N. A. Cherepkov, S. K. Semenov, C. W. McCurdy, T. N. Rescigno, C. L. Cocke, T. Osipov, S. Lee, M. H. Prior, A. Belkacem, A. L. Landers, H. Schmidt-Böcking, T. Weber and R. Dörner, *Science*, 2008, **320**, 920–923.
- 114 S. K. Semenov, M. S. Schöffler, J. Titze, N. Petridis, T. Jahnke, K. Cole, L. P. H. Schmidt, A. Czasch, D. Akoury, O. Jagutzki, J. B. Williams, T. Osipov, S. Lee, M. H. Prior, A. Belkacem, A. L. Landers, H. Schmidt-Böcking, T. Weber, N. A. Cherepkov and R. Dörner, *Phys. Rev. A*, 2010, **81**, 043426.
- 115 S. K. Semenov, V. V. Kuznetsov, N. A. Cherepkov, P. Bolognesi, V. Feyer, A. Lahmam-Bennani, M. E. Staicu Casagrande and L. Avaldi, *Phys. Rev. A*, 2007, **75**, 032707.
- 116 S. Motoki, J.-i. Adachi, Y. Hikosaka, K. Ito, M. Sano, K. Soejima, A. Yagishita, G. Raeev and N. A. Cherepkov, *J. Phys. B: At. Mol. Opt. Phys.*, 2000, **33**, 4193–4212.
- 117 N. A. Cherepkov, G. Raeev, J.-i. Adachi, Y. Hikosaka, K. Ito, S. Motoki, M. Sano, K. Soejima and A. Yagishita, *J. Phys. B: At. Mol. Opt. Phys.*, 2000, **33**, 4213–4236.
- 118 K. Ito, J.-i. Adachi, Y. Hikosaka, S. Motoki, K. Soejima, A. Yagishita, G. Raeev and N. A. Cherepkov, *Phys. Rev. Lett.*, 2000, **85**, 46.
- 119 V. V. Kuznetsov, S. K. Semenov and N. A. Cherepkov, *J. Chem. Phys.*, 2011, **134**, 134301.
- 120 T. Jahnke, L. Foucar, J. Titze, R. Wallauer, T. Osipov, E. P. Benis, A. Al-naser, O. Jagutzki, W. Arnold, S. K. Semenov, N. A. Cherepkov, L. P. H. Schmidt, A. Czasch, A. Staudte, M. S. Schöffler, C. L. Cocke, M. H. Prior, H. Schmidt-Böcking and R. Dörner, *Phys. Rev. Lett.*, 2004, **93**, 083002.
- 121 P. Bolognesi, V. Feyer, A. Lahmam-Bennani, M. E. S. Casagrande, L. Avaldi, S. K. Semenov, V. V. Kuznetsov and N. A. Cherepkov, *J. Electron Spectrosc. Relat. Phenom.*, 2007, **161**, 90–94.
- 122 H. Bachau, E. Cormier, P. Decleva, J. E. Hansen and F. Martín, *Rep. Prog. Phys.*, 2001, **64**, 1815–1942.
- 123 J. Rius i Riu, A. Karawajczyk, M. Stankiewicz, K. Yoshiki Franzén, P. Winiarczyk and L. Veseth, *Chem. Phys. Lett.*, 2001, **338**, 285–290.
- 124 L. Argenti, T. D. Thomas, E. Plésiat, X.-J. Liu, C. Miron, T. Lischke, G. Prümper, K. Sakai, T. Ouchi, R. Püttner, V. Sekushin, T. Tanaka, M. Hoshino, H. Tanaka, P. Decleva, K. Ueda and F. Martín, *New J. Phys.*, 2012, to be published.
- 125 E. Plésiat, L. Argenti, E. Kukk, C. Miron, K. Ueda, P. Decleva and F. Martín, *Phys. Rev. A*, 2012, **85**, 023409.
- 126 R. Polák and J. Fišer, *Chem. Phys.*, 2003, **290**, 177–188.
- 127 R. J. Gdanitz, *Chem. Phys. Lett.*, 1998, **283**, 253–261.
- 128 R. J. Le Roy, Y. Huang and C. Jary, *J. Chem. Phys.*, 2006, **125**, 164310.
- 129 J. B. West, K. Codling, A. C. Parr, D. L. Ederer, B. E. Cole, R. Stockbauer and J. L. Dehmer, *J. Phys. B: At. Mol. Opt. Phys.*, 1981, **14**, 1791–1801.
- 130 X. Li and J. Paldus, *J. Chem. Phys.*, 2008, **129**, 054104.
- 131 T. Aoto, K. Ito, Y. Hikosaka, A. Shibasaki, R. Hirayama, N. Yamamoto and E. Miyoshi, *J. Chem. Phys.*, 2006, **124**, 234306.
- 132 P. Baltzer, M. Larsson, L. Karlsson, B. Wannberg and M. C. Göthe, *Phys. Rev. A*, 1992, **46**, 5545.
- 133 E. Gagnon, P. Ranitovic, X.-M. Tong, C. L. Cocke, M. M. Murnane,

- H. C. Kapteyn and A. S. Sandhu, *Science*, 2007, **317**, 1374.
- 134 M. Ehara, H. Nakatsuji, M. Matsumoto, T. Hatamoto, X.-J. Liu, T. Lischke, G. Prümper, T. Tanaka, C. Makochekanwa, M. Hoshino, H. Tanaka, J. R. Harries, Y. Tamenori and K. Ueda, *J. Chem. Phys.*, 2006, **124**, 124311.
- 135 M. Ehara, K. Kuramoto, H. Nakatsuji, M. Hoshino, T. Tanaka, M. Kitajima, H. Tanaka, A. De Fanis, Y. Tamenori and K. Ueda, *J. Chem. Phys.*, 2006, **125**, 114304.
- 136 O. Nagy, C. P. Ballance, K. A. Berrington, P. G. Burke and B. M. McLaughlin, *J. Phys. B: At. Mol. Opt. Phys.*, 1999, **32**, L469–L477.
- 137 P. Baltzer, M. Lundqvist, B. Wannberg, L. Karlsson, M. Larsson, M. A. Hayes, J. B. West, M. R. F. Siggel, A. C. Parr and J. L. Dehmer, *J. Phys. B: At. Mol. Opt. Phys.*, 1994, **27**, 4915–4932.
- 138 K. Chakrabarti and J. Tennyson, *J. Phys. B: At. Mol. Opt. Phys.*, 2007, **40**, 2135–2145.
- 139 M. Eidelsberg, F. Launay, K. Ito, T. Matsui, P. C. Hinnen, E. Reinhold, W. Ubachs and K. P. Huber, *J. Chem. Phys.*, 2004, **121**, 292–308.
- 140 K. Ueda, M. Hoshino, T. Tanaka, M. Kitajima, H. Tanaka, A. De Fanis, Y. Tamenori, M. Ehara, F. Oyagi, K. Kuramoto and H. Nakatsuji, *Phys. Rev. Lett.*, 2005, **94**, 243004.
- 141 A. Thiel, J. Schirmer and H. Koppel, *J. Chem. Phys.*, 2003, **119**, 2088–2101.
- 142 U. Hergenhahn, *J. Phys. B: At. Mol. Opt. Phys.*, 2004, **37**, R89–R135.
- 143 M. Stener, D. Toffoli, G. Fronzoni and P. Decleva, *J. Chem. Phys.*, 2006, **124**, 114306.
- 144 A. Zangwill and P. Soven, *Phys. Rev. A*, 1980, **21**, 1561.
- 145 G. D. Mahan, *Phys. Rev. A*, 1980, **22**, 1780.
- 146 M. Stener, G. Fronzoni, D. Toffoli and P. Decleva, *Chem. Phys.*, 2002, **282**, 337–351.
- 147 D. Toffoli, M. Stener, G. Fronzoni and P. Decleva, *J. Chem. Phys.*, 2006, **124**, 214313.
- 148 D. Toffoli, P. Decleva, F. A. Gianturco and R. R. Lucchese, *J. Chem. Phys.*, 2007, **127**, 234317.
- 149 F. Martín, *J. Phys. B: At. Mol. Opt. Phys.*, 1999, **32**, R197.
- 150 C. T. Chen, Y. Ma and F. Sette, *Phys. Rev. A*, 1989, **40**, 6737–6740.
- 151 R. Püttner, I. Dominguez, T. J. Morgan, C. Cisneros, R. F. Fink, E. Rotenberg, T. Warwick, M. Domke, G. Kaindl and A. S. Schlachter, *Phys. Rev. A*, 1999, **59**, 3415.
- 152 V. Myrseth, J. D. Bozek, E. Kukk, L. J. Sæthre and T. D. Thomas, *J. Electron Spectrosc. Relat. Phenom.*, 2002, **122**, 57–63.
- 153 D. M. Barrus, R. L. Blake, A. J. Burek, K. C. Chambers and A. L. Prengner, *Phys. Rev. A*, 1979, **20**, 1045–1061.
- 154 J. Fernández, O. Fojón and F. Martín, *Phys. Rev. A*, 2009, **79**, 023420.
- 155 J. Fernández, F. L. Yip, T. N. Rescigno, C. W. McCurdy and F. Martín, *Phys. Rev. A*, 2009, **79**, 043409.
- 156 D. Akoury, K. Kreidi, T. Jahnke, T. Weber, A. Staudte, M. S. Schöffler, N. Neumann, J. Titze, L. P. H. Schmidt, A. Czasch, O. Jagutzki, R. A. Costa Fraga, R. E. Grisenti, R. Díez Muiño, N. A. Cherepkov, S. K. Semenov, P. Ranitovic, C. L. Cocke, T. Osipov, H. Adaniya, J. C. Thompson, M. H. Prior, A. Belkacem, A. L. Landers, H. Schmidt-Böcking and R. Dörner, *Science*, 2007, **318**, 949–952.
- 157 K. Kreidi, D. Akoury, T. Jahnke, T. Weber, A. Staudte, M. Schöffler, N. Neumann, J. Titze, L. P. H. Schmidt, A. Czasch, O. Jagutzki, R. A. Costa Fraga, R. E. Grisenti, M. Smolarski, P. Ranitovic, C. L. Cocke, T. Osipov, H. Adaniya, J. C. Thompson, M. H. Prior, A. Belkacem, A. L. Landers, H. Schmidt-Böcking and R. Dörner, *Phys. Rev. Lett.*, 2008, **100**, 13305.
- 158 O. Fojón, A. Palacios, J. Fernández, R. D. Rivarola and F. Martín, *Phys. Lett. A*, 2006, **350**, 371–374.
- 159 M. Arndt, O. Nairz, J. Vos-Andreae, C. Keller, G. van der Zouw and A. Zeilinger, *Nature*, 1999, **401**, 680.
- 160 N. Stolterfoht, B. Sulik, V. Hoffmann, B. Skogvall, J. Y. Chesnel, J. Rangama, F. Frémont, D. Hennecart, A. Cassimi, X. Husson, A. L. Landers, J. A. Tanis, M. E. Galassi and R. D. Rivarola, *Phys. Rev. Lett.*, 2001, **87**, 023201.
- 161 D. Misra, U. Kadhane, Y. P. Singh, L. C. Tribedi, P. D. Fainstein and P. Richard, *Phys. Rev. Lett.*, 2004, **92**, 153201.
- 162 O. Kamalou, J.-Y. Chesnel, D. Martina, J. Hanssen, C. R. Stia, O. Fojón, R. D. Rivarola and F. Frémont, *Phys. Rev. A*, 2005, **71**, 010702.
- 163 D. S. Milne-Brownlie, M. Foster, J. Gao, B. Lohmann and D. H. Madison, *Phys. Rev. Lett.*, 2006, **96**, 233201.
- 164 O. Fojón, J. Fernández, A. Palacios, R. D. Rivarola and F. Martín, *J. Phys. B: At. Mol. Opt. Phys.*, 2004, **37**, 3035–3042.
- 165 A. L. Landers, T. Weber, I. Ali, A. Cassimi, M. Hattass, O. Jagutzki, A. Nauert, T. Osipov, A. Staudte, M. H. Prior, H. Schmidt-Böcking, C. L. Cocke and R. Dörner, *Phys. Rev. Lett.*, 2001, **87**, 013002.